A hybrid upwind scheme for two-phase flow in fractured porous media

Enrico Ballini [a],*, Luca Formaggia [a], Alessio Fumagalli [a], Eirik Keilegavlen [b], Anna Scotti [a]

[a] *MOX, Department of Mathematics, Politecnico di Milano, Piazza Leonardo da Vinci 32, 20133 Milano, Italy*
[b] *Center for Modeling of Coupled Subsurface Dynamics, Department of Mathematics, University of Bergen, Norway*

ARTICLE INFO

ABSTRACT

Simulating the flow of two fluid phases in porous media is a challenging task, especially when fractures are included in the simulation. Fractures may have highly heterogeneous properties compared to the surrounding rock matrix, significantly affecting fluid flow, and at the same time hydraulic apertures that are much smaller than any other characteristic sizes in the domain. Generally, flow simulators face difficulties with counter-current flow, generated by gravity and pressure gradients, which hinders the convergence of non-linear solvers (Newton).

In this work, we model the fracture geometry with a mixed-dimensional discrete fracture network, thus lightening the computational burden associated to an equi-dimensional representation. We address the issue of counter-current flows with appropriate spatial discretization of the advective fluid fluxes, with the aim of improving the convergence speed of the non-linear solver. In particular, the extension of the hybrid upwinding to the mixed-dimensional framework, with the use of a phase potential upstreaming at the interfaces of subdomains.

We test the method across several cases with different flow regimes and fracture network geometries. Results show robustness of the chosen discretization and a consistent improvements, in terms of Newton iterations, compared to using phase potential upstreaming everywhere.

1. Introduction

Fluid flow and multiphase transport in fractured porous media are of critical importance for subsurface engineering: fractures may form major pathways for fluid flow, indeed, as fractures can have significantly higher permeability than the surrounding host rock, they may constitute the main pathways for fluid flow. Rapid flow through fracture networks can be a desired effect, for instance in the production of geothermal energy from hard rocks, but it may be detrimental for the storage of carbon dioxide and nuclear waste [1,2]. Moreover, for energy storage and production, fluid exchange between fractures and the host rock is important, while transport in fracture network also plays an important part in natural subsurface flows, including thermal convection, e.g., [3,4].

Numerical simulations are valuable tools to study and understand flow in fractured porous media, however, construction of adequate simulation models is challenging. The contrast in permeability between fractures and the host rock, together with the lack of scale separation in fracture length [5], imply that traditional upscaling is difficult for fluid flow, and even more so for transport processes. To classify the many models that have been developed to meet this challenge, it is useful to consider whether the fractures are represented explicitly or by equivalent continua [6]. In equivalent continuum models, fractures and host rock are

---

* Corresponding author.
  E-mail address: enrico.ballini@polimi.it (E. Ballini).

represented by one or multiple overlapping domains, with fluid flow taking place both within and possibly between the domains. Such continuum models can preserve the heterogeneity in flow properties between fractures and the host rock, however, estimating the transfer coefficients between the media may be challenging and they are effective only for "regular", i.e., evenly distributed, fracture networks [7–9]. Nevertheless, compared to alternative methods, continuum models have a relatively low computational cost, and variants thereof have been applied to large-scale simulations. In so-called embedded discrete fracture matrix models (EDFM), fractures are explicitly represented at the continuous level, but not in the computational grid, see for instance [10–12]. This results in simulation models that, in a sense, are very similar to those of continuum models, however, the explicit representation of fractures eases the calculation of the flow exchange between fractures and host rock. EDFM models have been developed to a high level of sophistication, see for instance [13].

Our main interest herein is the so-called discrete fracture matrix (DFM) models, which represent fractures explicitly in the computational grid. DFM models usually represent the fractures as lower-dimensional objects embedded in the host domain, resulting in a mixed-dimensional geometry [14–23]. In these models, equations and constitutive laws can be represented in the host rock, in fractures, and on the rock-fracture interface. This model is well suited when there is no clear separation of scales between the porous medium size, fracture size, and domain size [6]. Moreover, with a limited number of parameters, it can model the flow both along and across the fracture plane. The explicit representation of fractures can complicate grid construction and require a high number of grid cells, and thereby limit the domain size and number of fractures that can be included. Nevertheless, the detailed representation of the fracture network geometry makes DFM models ideally suited to study the interaction between physical processes such as flow and transport [24–27], and also mechanical deformation of fractures [28–30]. Particularly relevant to this work is the discretization of multiphase flow, which has been reported in, for instance, [17,19,22,31].

Multiphase flow in porous media can be described by a pressure equation which, in the assumption of negligible capillary pressure, has an elliptic character, combined with a set of transport equations that are essentially hyperbolic in nature [32]. For practical simulations, the equations are usually discretized by finite volume methods [33]. In particular, to avoid unphysical oscillations at the discrete level, phase mobilities have traditionally been discretized by upwinding each phase individually, using the so-called phase potential upstreaming (PPU) [34]. PPU is monotone and first order convergent, and often produces results that are reasonably accurate. However, for flow governed by a mixture of viscous and gravitational forces, the upstream direction assigned to each individual grid face in the discrete model is prone to flipping during Newton iterations, leading to convergence issues for the non-linear solver, e.g. [35].

To overcome these convergence problems, several improvements of nonlinear solvers can be used, including trust-region [36,37] and reordering methods [38,39]. Of interest to us herein is an approach that replaces the PPU treatment of mobilities with a discretization which is in a sense smoother, and thus less prone to changes in the upstream direction. Among the possible techniques to achieve such regularization, we focus our attention on the method known as hybrid upwinding (HU), which was developed in a series of papers [40–44]. At the core of the HU approach is the representation of the viscous flow by a total velocity field, with transport of individual phases taken as gravitational deviations from the total velocity. The total velocity is discretized with weighted averages of mobilities. Compared to PPU, HU possesses enhanced smoothness, which leads to significant improvements in the performance of the Newton solver, at the price of somewhat increased numerical diffusion.

In this work, we consider two phase flow for fractured porous media, and extend the HU approach to mixed-dimensional DFM models with explicit representation of fractures in the computational grid. Noting that HU applied to fracture networks in a capillary dominated regime has already been reported [43], we limit ourselves to the case of negligible capillary forces, and focus on the impact of viscous and gravitational effects. Compared to standard porous media, the presence of fracture networks introduces some additional difficulties, mainly the coupling among domains of different dimensions and the strong contrast in permeability, resulting in faster dynamics in the fracture network. Through a series of numerical experiments in two- and three-dimensional domains, we show that the extension of HU consistently outperforms PPU in terms of performance of a Newton solver. The computational gains increase with simulation complexity, indicating that our extension can be a key ingredient in enabling two-phase 3D DFM simulations in regimes where gravitational effects play an important role.

The paper is structured as follows: The governing equations are presented in Section 3, while in Section 4, we present the discretization methods with emphasis on the different approaches to upstreaming. Numerical tests are presented in Section 5, while Section 6 contains concluding remarks.

2. Domain representation

Due to the complexity of the mixed-dimensional representation, we devote this section to introduce and describe such framework. Starting from Section 2.1, we introduce some basic notations when the domain does not contain fractures. We extend the concepts in Section 2.2 when fractures are present and in Section 2.3 we discuss the strategy adopted for the coupling between objects of different dimensions.

2.1. Fracture-less domain

Let $\Omega \subset \mathbb{R}^d$, with $d = 2$ or 3, be a Lipschitz continuous domain representing the porous media when fractures are not present, with boundary $\partial\Omega$ and outer unit normal v. Being the problem time dependent, we consider the time interval $(0, T]$, with $T > 0$ the final time in [s], and introduce the space–time domain $\Omega^T = \Omega \times (0, T]$.
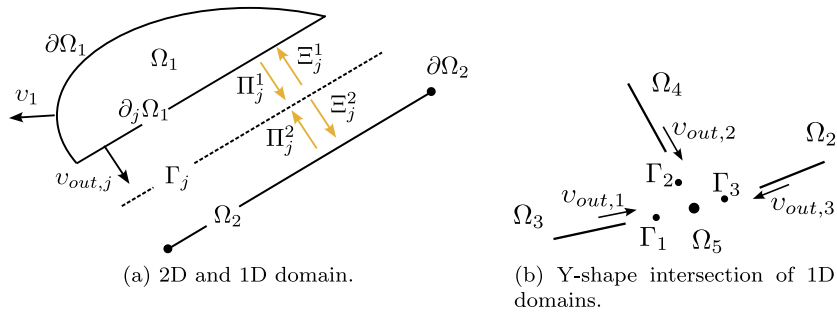
(a) 2D and 1D domain.

(b) Y-shape intersection of 1D domains.

Fig. 1. Mixed-dimensional domain. (a) Domains Ω_1 and Ω_2 are connected through the mortar interface Γ_j. (b) Example of three branches, in 3D fracture intersections and in 2D fractures, that intersect to a point Ω_5.

2.2. Fractured domain

We consider here the approach described in [6], where fractures are explicitly represented. Even for larger fractures, their thickness or aperture is orders of magnitude smaller than their typical lateral extensions. We thus approximate fractures with lower dimensional objects immersed in the rock domain. For simplicity, we assume that fractures are planar objects and we indicate with ϵ their thickness, in [m], assumed to be constant for each fracture.

The modeling of fractures leads to subdividing the whole domain $\Omega \subset \mathbb{R}^d$ into subdomains of different physical dimensions Ω_i, $i = 1, \ldots, I$, with I the total number of subdomains, such that $\overline{\Omega} = \cup_i \overline{\Omega}_i$ and $\Omega_i \cap \Omega_j = \emptyset$ for $i \neq j$. Each domain might represent the porous media, a fracture or a fracture intersection. For example, if $d = 3$, the subdomains representing the rock matrix have dimension 3, each reduced fracture has dimension 2, fracture intersections have dimension 1, and the possible intersection of intersections has dimension 0. If $d = 2$, then all the aforementioned dimensions should be scaled by 1. See Fig. 1 for an example of a mixed-dimensional domain.

2.3. Interface coupling

Flow in the subdomains Ω_i is interconnected through flux exchanges across the interface between domains with codimension equal to 1. We remark that there is no direct interaction between subdomains with codimension greater than 1, such as a 3D matrix rock and 1D intersection of fractures. We call these fluid fluxes *mortar fluxes* and can be interpreted as Lagrange multipliers that enforce the correct mass balance between subdomains [23,45]. In our formulation, we indicate the interface between domains, which we call *mortar interfaces* (or simply mortars) explicitly as Γ_j, $j = 1, \ldots, J$, with J the total number of mortars. This will be useful for the discretization approach presented in Section 4. See Fig. 1(a) for an illustration of a 2D matrix domain with one line fracture and a mortar domain interfacing the former domains.

On each subdomain Ω_i and mortar Γ_j the variables and data are marked by the subscript i or j, respectively. We indicate the mapping from the jth mortar Γ_j to the boundary of the related ith subdomain Ω_i by Ξ_j^i. We also introduce a map from a jth mortar Γ_j to a neighboring Ω_i, denoted by the symbol Π_j^i, see Fig. 1. These maps are relevant for the discrete problem, in particular when the meshes are non-conforming across subdomains and mortars, see Section 4.

For a subdomain Ω_i, the set of neighboring mortars is split into mortars, denoted by $\hat{S}_i$, that connect Ω_i to subdomains of higher dimension, and mortars that connect Ω_i to subdomains of lower dimensions, represented by the set $\check{S}_i$. Conversely, we denote by $\hat{R}_j$ the set of subdomains facing mortar Γ_j with $\dim(\Omega_i) > \dim(\Gamma_j)$, and with $\check{R}_j$ the set of subdomains facing the mortar Γ_j with $\dim(\Omega_i) = \dim(\Gamma_j)$. In the following, we use the abbreviation l to denote the indices of domains $\Omega_i \in \check{R}_j$, and, analogously, h to denote the indices of domains $\Omega_i \in \hat{R}_j$. Thus, for example, Π_j^h and Π_j^l are the maps from, respectively, $\Omega_i \in \hat{R}_j$ and $\Omega_i \in \check{R}_j$ towards the mortar Γ_j.

The normal at the boundaries is υ_i, whereas $\upsilon_{out,j}$ is the unit vector at the boundary of the higher dimensional domain, pointing outwards towards Γ_j. $\mathcal{N}_j$ is a map from $\overline{\Omega}$ to Γ_j such that, given $u : \overline{\Omega} \to \mathbb{R}$, we have $\mathcal{N}_j(u) : \overline{\Omega} \to \Gamma_j$. Its relevance will become apparent when we deal with the discretization procedure, where we give a more precise definition. With $\partial_j \Omega_i$ we indicate the boundary of Ω_i in contact with the mortar domain Γ_j. We denote the subdomain codimension extension with $\epsilon_i^{a_i}$, where $a_i = d - \dim(\Omega_i)$. For example, the codimension extension (thickness or aperture) of a planar fracture immersed in a 3D rock, would be $\epsilon^{3-2} = \epsilon$, while the codimension extension (area) of the intersection of two planar fractures would be $\epsilon^{3-1} = \epsilon^2$. Similarly, we define $b_j = d - \dim(\Gamma_j)$.

3. Mathematical model

In this part, we introduce the mathematical model considered for the two-phase flow. First, in Section 3.1 we present the model for a continuous medium without fractures. Subsequently, in Section 3.2 we discuss a dimensional analysis and obtain dimensionless groups, which are useful to set up the simulations in the examples. Finally, in Section 3.3 we present the mixed-dimensional model, an approach to approximate the fractures according to their features.

3.1. Continuous model

We assume no fractures and that in the void spaces of the porous media coexist two phases that fulfill the following assumptions: they are immiscible, isothermal, and non-reactive, with null capillary pressure. For their description, we consider the classical two-phase flow model in porous media, see [46–49] for more details. In the sequel, we will indicate with a subscript 0 and 1 data and variables associated to each phase.

The primary variables we consider in our model are the saturations $S_\ell : \Omega^T \to [0,1]$, which are dimensionless, for each phase $\ell = 0, 1$, and the pressure $p : \Omega^T \to \mathbb{R}$, in [Pa], equal for the two phases because of the assumption of null capillary pressure. The porous medium is characterized by the following properties: the porosity ϕ, that is dimensionless, and the intrinsic permeability of the rock K, in [m^2]. Each fluid phase is characterized by: the density ρ_ℓ, in [kg m^{-3}], the dimensionless relative permeability $k_{r,\ell} : [0,1] \to [0,1]$, dependent on the phase saturation S_ℓ, the dynamic viscosity μ_ℓ, assumed to be constant, in [Pa · s]. To simplify the notation, we introduce the phase mobility $\lambda_\ell = k_{r,\ell}/\mu_\ell$, in [Pa^{-1} s^{-1}]. We set g to be the gravity field constant assumed to be equal to 9.81[m s^{-2}], and we consider the vertical coordinate z pointing upwards, so the gravity vector is $-g\nabla z$. Finally, f_ℓ is a source or sink term associated to each phase ℓ, in [kg m^{-3} s^{-1}], possibly dependent on the saturation and the pressure.

The problem is to find (S_0, S_1, p) such that for $\ell = 0, 1$ we have

$$\begin{aligned} &\partial_t \phi(\rho_\ell S_\ell) + \nabla \cdot Q_\ell = f_\ell \\ &Q_\ell = -\rho_\ell \lambda_\ell K \left(\nabla p + \rho_\ell g \nabla z \right) \end{aligned} \quad \text{in } \Omega^T, \tag{1a}$$

where Q_ℓ, in [kg m^{-2} s^{-1}], is the mass flux of each phase, which is proportional to the gradient of the phase potential, Φ_ℓ, defined as

$$\Phi_\ell = p + \rho_\ell g z. \tag{1b}$$

Associated with the previous equations, in our numerical experiments we consider the following initial and boundary conditions

$$\begin{aligned} S_\ell(t=0, x) &= \overline{S}_\ell(x) &&\text{in } \Omega, \\ p(t=0, x) &= \overline{p}(x) &&\text{in } \Omega, \\ Q_\ell \cdot \upsilon &= 0 &&\text{on } \partial\Omega \times (0, T], \end{aligned} \tag{1c}$$

where $\overline{S}_\ell \in [0, 1]$, in [·], and $\overline{p}$, in [Pa], are given functions representing the initial values for the two phase saturation and pressure, respectively. We assume the following constraint for the saturations

$$S_0 + S_1 = 1 \quad \text{in } \Omega^T. \tag{1d}$$

We remark that we need to obey compatibility conditions between the data defining the problem. In particular the initial value of the saturation has to respect the constraint $\overline{S}_0 + \overline{S}_1 = 1$, and, for the given boundary conditions, steady state can only be reached when the source terms, f_ℓ, have zero average.

To close the system, we consider a constitutive equation to relate the phase density, assumed to be a liquid and thus nearly incompressible, with the pressure, and a model for the relative permeability, namely

$$\begin{aligned} \rho_\ell(p) &= \hat{\rho}_\ell e^{c_\ell(p-\hat{p})} \\ k_{r,\ell}(S_\ell) &= S_\ell^2 \end{aligned} \quad \text{in } \Omega^T, \tag{1e}$$

where $\hat{\rho}_\ell$ is a reference value for the density, in [kg m^{-3}], c_ℓ a phase specific compressibility, in [Pa^{-1}], and $\hat{p}$ a reference pressure value, in [Pa]. Different models can be employed such as the Brooks-Corey model for the saturation [50].

By using (1d), the problem (1) can be recast in an equivalent form in terms only of one saturation, here S_0, and pressure. Furthermore, we assume the porosity to be time independent and we replace one mass balance with the sum of the two mass balances. Thus, we replace (1a) and (1d) with

$$\begin{aligned} &\phi\partial_t[\rho_0 S_0 + \rho_1(1 - S_0)] + \nabla \cdot Q_T = f_T \\ &\phi\partial_t(\rho_0 S_0) + \nabla \cdot Q_0 = f_0 \end{aligned} \quad \text{in } \Omega^T, \tag{2a}$$

where $f_T = f_0 + f_1$, and Q_T is the total flux, defined as

$$Q_T = -\sum_{\ell=0,1} \rho_\ell \lambda_\ell K \left(\nabla p + \rho_\ell g \nabla z \right) \quad \text{in } \Omega^T, \tag{2b}$$

where λ_1 is now written as a function of S_0 instead of S_1. This formulation is useful to highlight the different nature of the variables, p and S_0, with consequent advantages in the discretization scheme, see Section 4. Indeed, problem (2) shows the so-called mixed parabolic-hyperbolic behavior if the compressibility is taken into account, an elliptic–hyperbolic behavior otherwise. As a consequence, the pressure varies smoothly while the saturation may be discontinuous in Ω [32,51].

3.2. Dimensional analysis

To describe the flow regime and compare the results of different simulations, we can scale the equations, initial and boundary conditions, and consequently obtain dimensionless groups. We denote by x_{ref} a reference value for the generic quantity x, the corresponding dimensionless variable is $\tilde{x} = x/x_{\text{ref}}$. At each physical variable or data we associate a reference value, some of them

might depend on each other as a consequence of the Pi theorem [52]. Neglecting the source term for simplicity, the mass balance becomes

$$\partial_{\tilde{t}}(\tilde{\phi}\tilde{\rho}_\ell S_\ell) + \frac{t_{\text{ref}}K_{\text{ref}}}{\phi_{\text{ref}}L_{\text{ref}}\mu_{\text{ref}}}\tilde{\nabla}\cdot\left[\tilde{\rho}_\ell\tilde{\lambda}_\ell\tilde{K}\left(\frac{p_{\text{ref}}}{L_{\text{ref}}}\tilde{\nabla}\tilde{p} + \rho_{\text{ref}}g_{\text{ref}}\tilde{\rho}_\ell\tilde{g}\tilde{\nabla}\tilde{z}\right)\right] = 0. \tag{3}$$

It governs the fluid motion in $\widetilde{\Omega^T} = \widetilde{\Omega}\times(0, T/t_{\text{ref}}]$, where $\widetilde{\Omega}$ is given by scaling each dimension of Ω by L_{ref}, with analogous initial and boundary condition of (1c). We set $t_{\text{ref}} = \phi_{\text{ref}}L_{\text{ref}}/u_{\text{ref}}$ and retrieve a reference velocity from a finite Darcy-type equation $u_{\text{ref}} = K_{\text{ref}}p_{\text{ref}}/(\mu_{\text{ref}}L_{\text{ref}})$, thus we set a reference pressure from viscous quantities $p_{\text{ref}} = \mu_{\text{ref}}^2/(K_{\text{ref}}\rho_{\text{ref}})$. Replacing them into (3), we obtain

$$\partial_{\tilde{t}}(\tilde{\phi}\tilde{\rho}_\ell S_\ell) + \tilde{\nabla}\cdot\left[\tilde{\rho}_\ell\tilde{\lambda}_\ell\tilde{K}\left(\tilde{\nabla}\tilde{p} + E_A\tilde{\rho}_\ell\tilde{g}\tilde{\nabla}\tilde{z}\right)\right] = 0, \tag{4}$$

where $E_A = \phi_{\text{ref}}\rho_{\text{ref}}^2 g_{\text{ref}}L_{\text{ref}}K_{\text{ref}}/\mu_{\text{ref}}^2$ is a dimensionless group that indicates the ratio of the effects of the gravity forces and the viscous forces. It can be seen as an Archimedes' number specific to two-phase flow problem driven by the gravity, or an adaptation of the gravity number [40,53,54] to scenarios where the reference velocity is ambiguous, such as the case of countercurrent flow driven by gravity.

3.3. A mixed-dimensional model

As mentioned before, when fractures are present we rely on dimensionally reduced models to approximate fractures with lower dimensional objects immersed in the rock domain. Consequently, we need to devise a new set of partial differential equation, derived from mass balance and Darcy law, that describe the flow in the fractures and the interaction with the rock matrix. The dimensional reduction by itself is well-established, and we refer to [14,55,56] for single phase flow and to [16,17,19,21,22] for two-phase flow. When this technique is combined with the representation of the geometry introduced in Section 2, we arrive at the following governing equations.

The flow problem is: find $(S_{0,i}, p_i)$ in each $\Omega_i^T = \Omega_i\times(0, T]$, $i = 1, \dots, I$ and $\zeta_{\ell,j}$ on each $\Gamma_j^T = \Gamma_j\times(0, T]$, $j = 1, \dots, J$, for both phases $\ell = 0, 1$, such that

$$\varepsilon_i^{a_i}\phi_i\partial_t[\rho_{0,i}S_{0,i} + \rho_{1,i}(1 - S_{0,i})] + \varepsilon_i^{a_i}\nabla\cdot Q_{T,i} + \sum_\ell\sum_{\Gamma_j\in\hat{S}_i}\Xi_j^i\mathcal{N}_j(\rho_\ell\lambda_\ell)\zeta_{\ell,j} = f_{T,i}, \tag{5a}$$

$$\varepsilon_i^{a_i}\phi_i\partial_t(\rho_{0,i}S_{0_i}) + \varepsilon_i^{a_i}\nabla\cdot Q_{0,i} + \sum_{\Gamma_j\in\hat{S}_i}\Xi_j^i\mathcal{N}_j(\rho_0\lambda_0)\zeta_{0,j} = f_{0,i}, \tag{5b}$$

with the following constitutive law for the mortar fluxes, $\zeta_{\ell,j}$,

$$\zeta_{\ell,j} - \varepsilon_l^{b_j-1}k_{\perp,j}\left\{\frac{2}{\varepsilon_l}[\Pi_j^h tr(p_h) - \Pi_j^l p_l] - \mathcal{N}_j(\rho_\ell)g\nabla z\cdot v_{out,j}\right\} = 0, \tag{5c}$$

and the following boundary conditions at all times to close the previous system:

$$\begin{aligned} Q_\ell|_{\partial_j\Omega_i}\cdot v_{out,j} - \Xi_j^h\mathcal{N}_j(\rho_\ell\lambda_\ell)\zeta_{\ell,j} = 0, &\qquad\forall j\in\check{S}_i \\ Q_\ell\cdot v|_{\partial\Omega_i} = 0, &\qquad\text{on }\partial\Omega_i\setminus\partial_j\Omega_i \end{aligned} \tag{5d}$$

Finally, appropriate initial conditions for the primary variables $S_{0,i}$, p_i and ζ_j have to be provided for all the domains Ω_i and mortars Γ_j.

The divergence and gradient in (5a) and (5b) are meant as being tangential to the manifold associated to the considered domain. Since we only consider flat subdomains, these operators can be easily written in local intrinsic orthogonal, and fixed, coordinates.

The additional terms in (5a) and (5b) compared to (2) are linked to the mortar fluxes and describe the interactions between domains of different dimensions.

Eq. (5c) derives from the flux described in (1a) along the orthogonal direction of the mortar Γ_j, where the pressure gradient is approximated by a finite difference across the subdomains. We recall that, in (5c), with the indeces l and h we denote $\varepsilon_l = \varepsilon_i, \Omega_i\in\check{R}_j$, $p_h = p_i$, $\Omega_i\in\hat{R}_j$, and $p_l = p_i$, $\Omega_i\in\check{R}_j$, tr is a trace operator, $k_{\perp,j}$ the normal permeability. In (5c), ζ_ℓ can be seen as a volumetric flux or velocity divided by the mobility, it is also used to compute the interface upwind direction as described below.

We call the formulation of the problem (5) dual-mortar formulation, where we name (5a) pressure equation and (5b) mass balance.

3.4. Manipulation of the model for discretization

The mass fluxes, $Q_{\ell,i}$ and $Q_{T,i} = Q_{0,i} + Q_{1,i}$, can be expressed differently, leading to different discretization methods, as we show in Section 4. The first straightforward option is to write $Q_{\ell,i} = \rho_{\ell,i}q_i$. Consequently,

$$Q_{T,i} = \rho_{0,i}q_{0,i} + \rho_{1,i}q_{1,i}, \tag{6}$$

where $q_{\ell,i}$ is the volumetric flux given by the Darcy law:

$$q_{\ell,i} = -\lambda_{\ell,i}K_i(\nabla p_i + \rho_{\ell,i}g\nabla z), \quad \ell = 0, 1 \tag{7}$$

This formulation is adopted in the phase-potential upwind (PPU) discretization, detailed in Section 4.3. Note that the physical properties of a fracture subdomain are now described by two quantities, the normal permeability, $k_{\perp,j}$ and the in-plane permeability K_i, that govern, respectively, the flow across and along the subdomain.

The second option separates the physical contribution of the fluxes, highlighting the one due to the pressure gradient, called viscous flux, and the one due to gravity. In this case, the total flux in the pressure Eq. (5a) is still written as the sum of the phases contribution, as in (6), while the flux Q_0 in the mass balance Eq. (5b) is further subdivided as

$$Q_{0,i} = V_{0,i} + G_{0,i}, \tag{8}$$

being $V_{0,i}$ the viscous mass flux and $G_{0,i}$ is the flux in mass due to gravity, as a result of the different densities of the fluids.

$$V_{0,i} = \rho_{0,i} \frac{\lambda_{0,i}}{\lambda_{T,i}} (q_{0,i} + q_{1,i}) \tag{9}$$

$$G_{0,i} = \rho_{0,i} K_i \frac{\lambda_{0,i} \lambda_{1,i}}{\lambda_{T,i}} (\rho_{1,i} - \rho_{0,i}) g \nabla z \tag{10}$$

with $\lambda_{T,i} = \lambda_{0,i} + \lambda_{1,i}$ the total mobility, in $[\mathrm{Pa\,s^{-1}}]$. This second formulation is adopted in the hybrid upwind (HU) discretization, detailed in Section 4.4.

At the discrete level, we need that the operator $\mathcal{N}_j$ that maps variables from domains Ω_i to an adjacent mortar domain Γ_j has an upwinding nature, to avoid the appearance of spurious oscillations. To this purpose, we use the following formulation:

$$\mathcal{N}_j(u_\ell) = \begin{cases} \Pi_j^i u_{\ell,i} & \text{if } \zeta_{\ell,j} < 0, \\ \Pi_j^i tr(u_{\ell,i}) & \text{if } \zeta_{\ell,j} \geq 0, \end{cases} \tag{11}$$

where $u_{\ell,i}$ is defined in $\Omega_i \in \check{R}_j$ in the first case, and $u_{\ell,i}$ is defined in $\Omega_i \in \hat{R}_j$ in the second case. Because of the absence of internal fluxes, zero-dimensional domains should be treated carefully. For each zero-dimensional Ω_i, for $k = 1, \ldots, I$ and for both phases $\ell = 0, 1$, the mass balances reduce to finding $(S_{0,i}, p_i)$ such that

$$\varepsilon^{a_i} \phi_i \partial_t [\rho_{0,i} S_{0,i} + \rho_{1,i}(1 - S_{0,i})] + \sum_\ell \sum_{\Gamma_j \in \hat{S}_i} \Xi_j^i \mathcal{N}_j(\rho_\ell \lambda_\ell) \zeta_{\ell,j} = f_{T,i},$$

$$\varepsilon^{a_i} \phi_i \partial_t (\rho_{0,i} S_{0,i}) + \sum_{\Gamma_j \in \hat{S}_i} \Xi_j^i \mathcal{N}_j(\rho_0 \lambda_0) \zeta_{0,j} = f_{0,i}. \tag{12}$$

See Fig. 1(b) for an example of the intersection of three branches.

We model the fluid mobility with a quadratic dependence on the saturation:

$$\lambda_\ell = S_\ell^2. \tag{13}$$

4. Discretization

In this section, we present the considered approach to solve system (5) numerically. The main numerical challenge is how to approximate the non-linear advective part appropriately since it is composed by multiple terms that might act quite differently. This has an impact also on the convergence of the Newton method chosen to solve the resulting non-linear problem.

After a brief introduction to the discretization tools in Section 4.1, we will present the first discretization method in Section 4.3, which will be referred as PPU. The second discretization method, which is one of the original contribution of this work, is an extension to the mixed-dimensional framework of the hybrid upwind scheme and its application to the case of fractured media [40–42,44,57–59]. It is presented in Section 4.4 and it is referred as HU. The aim of this method is address the countercurrent flow problem more effectively, reducing the number of Newton iterations required to solve the non-linear system at each timestep.

4.1. Common setup

The subdomains Ω_i and mortars Γ_j are approximated with grids composed of simplex or hexahedron cells $\mathfrak{c}$ of characteristic size $h_\mathfrak{c}$ and Lebesgue measure $|\mathfrak{c}|$. The faces of a cell $\mathfrak{c}$ are denoted by $\mathfrak{f}$. Each face between two cells $\mathfrak{c}_m$ and $\mathfrak{c}_n$ is associated with a unit normal $\hat{v}_{mn}$. We denote by $adj(\mathfrak{c}_m)$ the neighboring cells of $\mathfrak{c}_m$ within the same domain. The formulation with mortar fluxes let us easily deal with non-conforming meshes across the interfaces between domains of different dimensions, as depicted in Fig. 2.

We solve (5) by discretizing the equations with a cell centered finite volume method [60,61].

In the following, we indicate with x_{mn} the evaluation of a generic variable, x, on the face $\mathfrak{f}$ between cells $\mathfrak{c}_m$ and $\mathfrak{c}_n$. Moreover, we denote the jump of a variable x between two cells $\mathfrak{c}_m$ and $\mathfrak{c}_n$ as $\Delta x_{mn} = x_m - x_n$. Before continuing, we define the discrete upwind operator $\mathcal{M}$ between $\mathfrak{c}_m$ and $\mathfrak{c}_n$ with respect to an upstream direction v_{mn} and the oriented segment $\overline{mn}$ that connects the cell centers from $\mathfrak{c}_m$ to $\mathfrak{c}_n$:

$$\mathcal{M}(x_m, x_n; v_{mn}) = \begin{cases} x_m & \text{if } v_{mn} \cdot \overline{mn} \geq 0, \\ x_n & \text{if } v_{mn} \cdot \overline{mn} < 0. \end{cases}$$
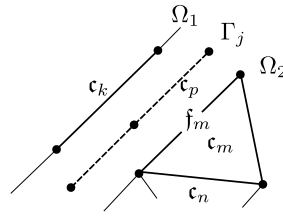
Fig. 2. Grid elements of a 1D domain, Ω_1 facing a 2D domain, Ω_2, and mortar, Γ. Any cell is denoted by $\mathfrak{c}$, while the faces, i.e., the boundary of $\mathfrak{c}$ are $\mathfrak{f}$.

Similarly, the component of a variable $\underline{x}$ projected on a cell $\mathfrak{c}_p$ of the mortar Γ_j with the interface upwind defined in (11), according to the upstream direction v_p defined on the mortar cell $\mathfrak{c}_p$, is computed as:

$$[\mathcal{N}_j(\underline{x}; v_p)]_p = \begin{cases} \Pi^i_{j,pk} x_k & \text{if } v_p < 0, \ x_k \in \Omega_i \in \check{R}_j, \\ \Pi^i_{j,pn} x_n & \text{if } v_p \geq 0, \ x_n \in \Omega_i \in \hat{R}_j, \ n \in S^{\mathfrak{c}}_j, \end{cases}$$

where $S^{\mathfrak{c}}_j$ is the set of indices n denoting the cells of Ω_i at the boundaries facing Γ_j. To ease notation, from now on we denote $[\mathcal{N}_j(\underline{x}; v_p)]_p$ as x^v_p.

A remark should be made for the discrete maps, Π and Ξ, in particular when a non-matching discretization is used between objects of different dimensions. To achieve maximum accuracy, in the case of cell-wise constant variables as are applied herein, the map for intensive variables (e.g. the pressure) should apply area-weighted averaging, while extensive quantities (e.g. fluxes) should be summed.

Let us consider a cell $\mathfrak{c}_p \in \Gamma_j$, a cell $\mathfrak{c}_k \in \Omega_i \in \check{R}_j$ and a boundary face $\mathfrak{f}_m$ of cell $\mathfrak{c}_m \in \hat{R}_j$, see Fig. 2. Let l_{mp} and l_{kp} be the overlap surface between boundary face $\mathfrak{f}_m$ and cell $\mathfrak{c}_p$, and cell $\mathfrak{c}_k$ and cell $\mathfrak{c}_p$, respectively. For the intensive variable we have: $\Pi^{h,ave}_{j,mp} = l_{mp}/|\mathfrak{c}_p|$ and $\Pi^{l,ave}_{j,kp} = l_{kp}/|\mathfrak{c}_p|$, while for an extensive variable: $\Pi^{h,sum}_{j,mp} = l_{mp}/|\mathfrak{f}_m|$ and $\Pi^{l,sum}_{j,kp} = l_{kp}/|\mathfrak{c}_k|$. Similarly for Ξ. To ease the notation, we will not specify the type of map, it should be clear from the context. As mentioned before, it is worth noting that the faces and cells facing mortars are, in general, non-conforming, as depicted in Fig. 2. The dual-mortar formulation allows us to easily handle such meshes, which could arise from a study of geometrical variability, as shown in [62].

4.2. Finite volume method

For the sake of clarity, we present in this section the main concepts of the finite volume discretization method. We consider a generic balance equation for a property x of a material point in moving matter on a compact subset ω of Ω, with fixed boundaries $\partial\omega$.

$$\frac{d}{dt} \int_\omega x = -\int_{\partial\omega} F_x + \int_\omega \psi_x.$$

where F_x is the flux of x through the boundaries $\partial\omega$ and ψ_x is a source term. Being x associated with the particle of matter moving at velocity u, we have $F_x = xu \cdot v$. Defining $f_x := xu$, we have

$$\frac{d}{dt} \int_\omega x = -\int_{\partial\omega} f_x \cdot v + \int_{\partial\omega} \psi_x, \tag{14}$$

which is the formulation used to discretize equations with the finite volume approach. Assuming sufficient regularity of the integrands we can apply the divergence theorem, and, due to the arbitrariness of ω, the balance equation must hold in its strong form,

$$\partial_t x + \nabla \cdot f_x = \psi_x, \quad \text{in } \Omega, \tag{15}$$

which is the form we used to present the partial differential equation for the mass balances for the phases $\ell = 0, 1$ in (1).

The finite volume method strictly follows the physics by applying (14) to several non-intersecting regions, the cells $\mathfrak{c}_m$ of the computational grid, treated in Section 4.1. We adopted a cell-centered finite volume method [60,61]. Let x_m be the mth d.o.f. (component) of a generic discrete primary variable $\underline{x}$, and similarly for the source term $\psi_{x,m}$. Let $F_{x,mn}$ be the component of the discrete counterpart of the flux $f_x \cdot v$ in (14) at the face between two adjacent cells $\mathfrak{c}_m$ and $\mathfrak{c}_n$. Moreover, let $\overline{F}_{x,mn} := |\mathfrak{f}_{mn}| F_{x,mn}$ be the *integrated numerical flux*, or simply *numerical flux* or *flux* whenever it is clear from the context. Note that $F_{x,mn}$ and $\overline{F}_{x,mn}$ are quantities associated with the faces $\mathfrak{f}_{mn}$ while the d.o.f.s are associated with the cell centers.

By applying the integration on a cell we have

$$|\mathfrak{c}_m| \frac{dx_m}{dt} + \sum_{\mathfrak{c}_n \in \text{adj}(\mathfrak{c}_m)} \overline{F}_{x,mn} = |\mathfrak{c}_m| \psi_{x,m}.$$

Dividing by the cell volume

$$\frac{dx_m}{dt} + \frac{1}{|\mathfrak{c}_m|} \sum_{\mathfrak{c}_n \in \text{adj}(\mathfrak{c}_m)} |\mathfrak{f}_{mn}| F_{x,mn} = \psi_{x,m}. \tag{16}$$

Eq. (16) strictly resembles the differential form (15), where the term $\frac{1}{|\mathfrak{c}_m|} \sum_{\mathfrak{c}_n \in \text{adj}(\mathfrak{c}_m)} |\mathfrak{f}_{mn}|$ is the discrete equivalent of the continuous divergence, $\nabla \cdot () = \lim_{\omega \to 0} \frac{\int_{\partial \omega} () \cdot \upsilon}{\omega}$, with the right units $[\text{m}^{-1}]$.

In the following, we present the discrete equations following (16) to have almost a one-to-one correspondence with their continuous counterparts, facilitating the interpretation of the terms.

We remark that the numerical fluxes are quantities associated with the faces, while the d.o.f.s are associated with the cell centers. This necessitates averaging or interpolating the variables to determine their values at the faces. For a hyperbolic problem, it is common practice to use a one-sided or *upwind* strategy to compute the variable at the faces, thus avoiding the rise of numerical oscillations [60,61].

4.3. Standard upwinding

Let $S_i^{\mathfrak{f}}$ be the set of indices for faces $\mathfrak{f}$ on the boundary towards Γ_j and let $\circ$ be the element-wise (Hadamard) product. The discrete primary variables, i.e. the degrees of freedom (d.o.f.) associated to the cell centers, are the components of the vectors $\underline{p}_i$, $\underline{S}_{0,i}$ for the subdomains Ω_i and $\underline{\zeta}_{0,j}$, $\underline{\zeta}_{1,j}$ at the mortars Γ_j. The discretization in space of (5) with fluxes from (6) and (7), reads for $\ell = 0, 1$

$$
\begin{aligned}
\varepsilon_i^{a_i} \partial_t (\underline{u}_{0,i} + \underline{u}_{1,i}) + \varepsilon_i^{a_i} \underline{\underline{D}} \, \underline{Q}_{T,i}^{PPU} + \underline{\psi}_i^p &= 0, && \text{in } \Omega_i, \\
\varepsilon_i^{a_i} \partial_t \underline{u}_{0,i} + \varepsilon_i^{a_i} \underline{\underline{D}} \, \underline{Q}_0^{PPU} + \underline{\psi}_i^s &= 0, && \text{in } \Omega_i, \\
\underline{\zeta}_{\ell,j} - \varepsilon_l^{b_j - 1} k_{\perp,j} |\underline{\mathfrak{c}}_j| \circ \left[\frac{1}{\varepsilon_l/2} (\underline{\underline{\Pi}}_j^h \underline{\text{tr}}(\underline{p}_h) - \underline{\underline{\Pi}}_j^l \underline{p}_l) - \underline{\rho}_\ell^{\zeta_{\ell,j}} g \nabla z \cdot \upsilon_{out,j} \right] &= 0, && \text{in } \Gamma_j \, .
\end{aligned}
\tag{17}
$$

The discrete boundary conditions, for each vector element k, are given by:

$$
\begin{aligned}
Q_{\ell,i,k}^{PPU} - \Xi_{j,km}^i \rho_{\ell,m}^{\zeta_{\ell,j}} \lambda_{\ell,m}^{\zeta_{\ell,j}} \zeta_{\ell,j,m} &= 0, \quad k \in S_i^{\mathfrak{f}}, \\
Q_{\ell,i,k}^{PPU} &= 0, \qquad\qquad \text{otherwise.}
\end{aligned}
$$

To ease the notation, in what follows, we drop the subscript denoting subdomain and interfaces and let relations hold for each subdomain Ω_i or mortar Γ_j.

The terms of the accumulation variables are $u_{0,m} = \phi_m \rho_{0,m} S_{0,m}$, and $u_{1,m} = \phi_m \rho_{1,m}(1 - S_{0,m})$. The elements of discrete divergence operator $\underline{\underline{D}}$ are defined as:

$$
D_{mn} = \frac{1}{|\mathfrak{c}_m|}
\begin{cases}
1 & \text{if } \mathfrak{c}_n \in adj(\mathfrak{c}_m) \text{ and } \hat{\upsilon}_{mn} \text{ points inwards } \mathfrak{c}_m, \\
-1 & \text{if } \mathfrak{c}_n \in adj(\mathfrak{c}_m) \text{ and } \hat{\upsilon}_{mn} \text{ points outwards } \mathfrak{c}_m, \\
0 & \text{if } \mathfrak{c}_n \notin adj(\mathfrak{c}_m).
\end{cases}
$$

Note that the units of D_{mn} are $\text{m}^{-\dim \Omega_i}$, and its definition here slightly differs from what stated in Section 4.2. The integrated-normal mass flux $Q_{\ell,mn}^{PPU} = \rho_{\ell,mn}^{PPU} q_{\ell,mn}^{PPU}$ is discretized adopting an upwind scheme whose upstream direction is linked to the phase potential, Φ_ℓ, (1b). In particular, we have: $\rho_{\ell,mn}^{PPU} = \mathcal{M}(\rho_{\ell,m}, \rho_{\ell,n}; \tilde{q}_{\ell,mn})$, where $\tilde{q}_{\ell,mn}$ represents the phase potential multiplied by the transmissibilities. It is computed as

$$
\underline{\tilde{q}}_\ell = \underline{\underline{T}} \, \underline{p} + \underline{\underline{T}}^g g \underline{\rho}_\ell \circ \underline{z},
$$

where $\underline{\underline{T}}$ and $\underline{\underline{T}}^g$ are the transmissibilities, that depend on the permeability K and the grid element geometry. Note that the elements of $\underline{\tilde{q}}_\ell$ are $\tilde{q}_{\ell,mn}$, i.e., quantities evaluated at the faces. In the present work, $\underline{\underline{T}}$ is computed with the multi-point flux approximation (MPFA) [63,64] for its property of being consistent using non K-orthogonal grids [63,65], although other methods could be used, such as the two point flux approximation (TPFA) [63,66]. $\underline{\underline{T}}^g$ is the consistent transmissibility for the gravity term, its determination is explained in [67]. The integrated volumetric flux is: $q_{\ell,mn}^{\overline{PPU}} = \lambda_{\ell,mn}^{PPU} \tilde{q}_{\ell,mn}$, where $\lambda_{\ell,mn}^{PPU}$ are phase mobility defined as $\lambda_{\ell,mn}^{PPU} = \mathcal{M}(\lambda_{\ell,m}, \lambda_{\ell,n}; \tilde{q}_{\ell,mn})$. The elements of the source term, $\underline{\psi}^p$ in the pressure equation and $\underline{\psi}^s$ in the mass balance for the phase 0 are respectively given by

$$
\psi_m^p = \frac{1}{|\mathfrak{c}_m|} \sum_\ell \sum_{\Gamma_j \in \hat{S}} \Xi_{j,mn}(\rho_{\ell,n}^{\zeta_{\ell,j}} \lambda_{\ell,n}^{\zeta_{\ell,j}} \zeta_{\ell,j,n}) - f_{\ell,m},
$$

$$
\psi_m^s = \frac{1}{|\mathfrak{c}_m|} \sum_{\Gamma_j \in \hat{S}} \Xi_{j,mn}(\rho_{0,n}^{\zeta_{0,j}} \lambda_{0,n}^{\zeta_{0,j}} \zeta_{0,j,n}) - f_{0,m}.
$$

Regarding the constitutive law associated with the mortar fluxes, we highlight that it is not a partial differential equation but an algebraic expression, so no spatial discretization scheme is required.

4.4. Hybrid upwind

The semi-discrete in space counterpart of the problem (5), with fluxes from (6), (7) for the pressure Eqs. (5a) and (8) for the mass balance Eq. (5b), is given by for $\ell = 0,1$

$$\varepsilon_i^{a_i} \partial_t(\underline{u}_{0,i} + \underline{u}_{1,i}) + \varepsilon_i^{a_i} \underline{\underline{D}}\, \underline{Q}_{T,i}^{HU} + \underline{\psi}_i^p = 0, \qquad \text{in } \Omega_i, \tag{18a}$$

$$\varepsilon_i^{a_i} \partial_t \underline{u}_{0,i} + \varepsilon_i^{a_i} \underline{\underline{D}}\left(\underline{V}_{0,i} + \underline{G}_{0,i}\right) + \underline{\psi}_i^s = 0, \qquad \text{in } \Omega_i, \tag{18b}$$

$$\underline{\zeta}_{\ell,j} - \varepsilon_l^{b_j-1} k_{\perp,j} |\underline{\varsigma}_j| \circ \left[\frac{1}{\varepsilon_l/2}(\underline{\underline{\Pi}}_j^h \underline{\mathrm{tr}}(\underline{p}_h) - \underline{\underline{\Pi}}_j^l \underline{p}_l) - \underline{\rho}_\ell^{\zeta_{\ell,j}} g \nabla z \cdot v_{out,j}\right] = 0, \qquad \text{in } \Gamma_j. \tag{18c}$$

Concerning the different nature of the pressure Eq. (5a) and mass balance (5b), they are discretized adopting different strategies. The variables defining $\underline{Q}_T^{HU}$ are discretized with a blended method that smoothly switches from a centered scheme to an upwind scheme, according to the intensity of the jump of the phase potential evaluated at each face. Conversely, the fluxes in the mass balance are discretized with a pure upwind scheme as described below. In particular, by dropping the domain index, we have

$$Q_{T,mn}^{HU} = \sum_{\ell=0,1} \rho_{\ell,mn} q_{\ell,mn}^{WA}, \tag{19}$$

where the densities are averaged at the faces according to the saturation:

$$\rho_{\ell,mn} = \frac{S_{\ell,m}\rho_{\ell,m} + S_{\ell,n}\rho_{\ell,n}}{S_{\ell,m} + S_{\ell,n}},$$

and the discrete volumetric fluxes integrated along the faces, $q_{\ell,mn}^{WA}$, are computed following [44]. For the reader convenience, we report here the main steps. The discrete volumetric normal flux, $q_{\ell,mn}^{WA}$, incorporates the grid and rock properties, the fluid properties, and it is proportional to the phase potential:

$$q_{\ell,mn}^{WA} = \lambda_{mn}^{WA} T_{mn} \Delta\Phi_{\ell,mn}, \tag{20}$$

where, in the present work we strictly follow the method proposed in [44], the transmissibilities T_{mn} are computed with the TPFA. Nevertheless, other methods, as MPFA, could be used with minor modifications. The jump of the phase potential is defined as

$$\Delta\Phi_{\ell,mn} = \Delta p_{\ell,mn} + \rho_{\ell,mn} g \Delta z_{mn},$$

where z_m and z_n of Δz_{mn} are the z-coordinates of the centroid of the corresponding cells. The mobilities λ_{mn}^{WA} are the core of the blended centered-upwind scheme: they are the weighted average (WA) dependent solution of the mobilities computed at the cells:

$$\lambda_{\ell,mn}^{WA} = \beta_{\ell,mn} \lambda_{\ell,m} + (1 - \beta_{\ell,mn}) \lambda_{\ell,n}$$

where the weight $\beta_{\ell,mn} \in [0,1]$ is an increasing function of the jump of the phase potential $\Delta\Phi_{\ell,mn}$:

$$\beta_{\ell,mn} = 0.5 + \frac{1}{\pi} \arctan(c_{\ell,mn} \Delta\Phi_{\ell,mn}),$$

with $c_{\ell,mn}$ a coefficient that depends on the grid and fluid properties

$$c_{\ell,mn} = \min\left(\frac{(k_{r,\ell}(1))^{-1} \max_{S_\ell} |k_{r,\ell}''(S_\ell)|}{\max_\ell(\rho_{\ell,mn}) g \Delta z_{mn}}, 10^6\right).$$

We remind that $k_{r,\ell}$ is the relative permeability of phase ℓ. Details about $\beta_{\ell,mn}$ can be found in [44].

The fluxes in the mass balance are discretized with an upwind scheme to honor the hyperbolicity of the equation. Since the motion of the fluid is forced by two main physical driving forces, one related to the pressure gradient and the other linked to the gravity field, these two quantities are treated differently to upwind the variables. The discretization of the viscous flux is a one-sided scheme that considers the total velocity as upwind direction:

$$V_{0,mn} = \rho_{0,mn}^V \frac{\lambda_{0,mn}^V}{\lambda_{T,mn}^V} q_{T,mn}$$

where $\rho_{0,mn}^V = \mathcal{M}(\rho_{0,m}, \rho_{0,n}; q_{T,mn})$ and similarly for $\lambda_{0,mn}^V$ and $\lambda_{T,mn}^V$. The total volumetric flux (or total velocity), $q_{T,mn} = q_{0,mn} + q_{1,mn}$, is computed from (20).

The gravity flux $G_{0,mn}$ is computed with a one-sided scheme with the upwind direction dependent on the gravity effects. In particular, we have

$$G_{0,mn} = \rho_{0,mn}^G q_{0,mn}^G,$$

where the upstream direction for the density is the volumetric flux due to the gravity effects, $\rho_{0,mn}^G = \mathcal{M}(\rho_{0,m}, \rho_{0,m}; q_{0,mn}^G)$. The volumetric flux, $q_{0,mn}^G$, is computed as:

$$q_{0,mn}^G = T_{mn} \frac{\lambda_{0,mn}^G \lambda_{1,mn}^G}{\lambda_{T,mn}^G}(\rho_{0,mn} - \rho_{1,mn}) g \Delta z_{mn} \tag{21}$$

where $\lambda_{0,mn}^G = \mathcal{M}(\lambda_{0,m}, \lambda_{0,n}; \omega_{0,mn})$ and analogously for the other mobilities. The function $\omega_{\ell,mn}$ describes the gravity effects acting on fluids with different densities:

$$\omega_{\ell,mn} = \lambda_{k,mn}^g \left((\rho_{k,mn} - \rho_{\ell,mn})g\Delta z_{mn} \right),$$

where the upwinded mobility is given by

$$\lambda_{k,mn}^g = \begin{cases} \lambda_{k,m} & \text{if } \rho_{k,mn} < \rho_{\ell,mn}, \\ \lambda_{k,n} & \text{if } \rho_{k,mn} \geq \rho_{\ell,mn}. \end{cases}$$

Further details can be found in [44].

The constitutive laws of the mortar fluxes, (5c), do not evidence the different behavior of the pressure and saturation variables. As in the PPU approach, no particular discretization method is required. Future developments regard the study of a pressure-mass formulation of the mortar fluxes constitutive laws and a suitable discretization method.

The spatial order of convergence of the discretization of the fluxes Q_T^{HU}, V_0, and G_0 is at most one for smooth solutions [41]. The discretization of the mortar fluxes is expected to be of order one since an error proportional to h_c is introduced with the approximation of $\mathcal{N}_j$. This occurs because no trace reconstruction is used to retrieve the value of x on $\partial_j \Omega_i$, instead, the value at the cell center is used. Thus, we expect the spatial order of convergence of the discretization scheme to be at most one for smooth solutions. A numerical verification is performed in Section 5.1.

4.5. Time discretization and numerical details

For the time marching, we use the implicit Euler scheme for its well known stability properties that allow us to use large timesteps.

We call $\underline{x}$ the vectors of the discrete primary variables,

$\underline{x} = [\underline{S}_1^T \dots \underline{S}_i^T, \dots \underline{S}_I^T, \underline{p}_1^T, \dots, \underline{p}_i^T \dots, \underline{p}_I^T, \underline{\zeta}_{0,1}^T, \dots, \underline{\zeta}_{0,j}^T \dots \underline{\zeta}_{0,J}^T, \underline{\zeta}_{1,1}^T, \dots \underline{\zeta}_{1,j}^T, \dots \underline{\zeta}_{1,J}^T]^T$. The system (18), and analogously for (17), after the time discretization at timestep n of size dt, can be written in the compact form $\underline{R}^{n+1} = 0$, where

$$\underline{R}^{n+1} = \frac{\underline{U}^{n+1} - \underline{U}^n}{dt} + \underline{F}^{n+1}. \tag{22}$$

Here,

$$\underline{U}^n = \begin{bmatrix} \dots \\ \varepsilon_i^{a_i}(\underline{u}_{0,i}(\underline{x}^n) + \underline{u}_{1,i}(\underline{x}^n)) \\ \dots \\ \varepsilon_i^{a_i}\underline{u}_{0,i}(\underline{x}^n) \\ \dots \\ 0 \end{bmatrix}, \quad \underline{F}^n = \begin{bmatrix} \dots \\ \varepsilon_i^{a_i}\underline{\underline{D}}\,\underline{Q}_{T,i}^{HU}(\underline{x}^n) + \underline{\psi}_i^p(\underline{x}^n) \\ \dots \\ \varepsilon_i^{a_i}\underline{\underline{D}}\left(\underline{V}_{0,i}(\underline{x}^n) + \underline{G}_{0,i}(\underline{x}^n)\right) + \underline{\psi}_i^s(\underline{x}^n) \\ \dots \\ E \end{bmatrix}, \quad \forall i, j,$$

where E is the left hand side of Eq. (18c).

The implicit method leads to the system of discrete non-linear equations (22) to be solved at each time step, which is solved with the Newton method.

Its kth iteration takes the form

$$\underline{\underline{J}}_k^{n+1}\delta\underline{x}_k = -\underline{R}_k^{n+1},$$
$$\underline{x}_{k+1}^{n+1} = \underline{x}_k^{n+1} + \delta\underline{x}_k,$$

where $\underline{\underline{J}}_k^{n+1}$ is the Jacobian of $\underline{R}_k^{n+1}$. Note that the Newton method requires the knowledge of the Jacobian, which changes, at each iteration.

Several methods can be adopted for the computation of the Jacobian or its approximation, such as a finite difference, complex step [68,69] or automatic differentiation [70]. We adopt the latter, which is exact up to machine precision.

In case of convergence failure of Newton method, the time step is halved and the iterative method is restarted to the previous step. After achieving Newton convergence, the timestep is restored to its initial fixed value. The procedure is repeated till convergence is reached or the time step becomes excessively small for a practical application and it is thus stopped due to lack of convergence. We set the threshold for the timestep to be $dt_{min} = 10^{-12}$.

The discretization method needs to comply with the constraint on the saturation, that is $S_\ell \in [0, 1]$. We force its enforcement by clipping the saturation value after each Newton iteration.

We implement the discretization methods in PorePy, a simulation tool for fractured and deformable porous media suited for the mixed-dimensional problem [71].

The pseudo-code to run a simulation is described in Algorithm 1

Algorithm 1 Full simulation procedure

given $\underline{x}^0$, dt_0, geometry
1: generate mixed-dimensional grid
2: **while** $t < T$:
3:     **while** $err > tol \wedge k < k_{max}$:
4:         compute $\underline{\underline{J}}_k^{n+1}$ and $\underline{R}_k^{n+1}$
5:         solve $\underline{\underline{J}}_k^{n+1}\delta\underline{x}_k = -\underline{R}_k^{n+1}$
6:         update $\underline{x}_{k+1}^{n+1} = \underline{x}_k^{n+1} + \delta\underline{x}_k$
7:         clip saturation
8:         compute *err*
9:         $k \leftarrow k + 1$
10:    $n \leftarrow n + 1$
11:    **if** $k = k_{max}$:
12:        $dt \leftarrow dt/2$
13:    **else**:
14:        $t \leftarrow t + dt$
15:        $dt = dt_0$
16:        save $\underline{x}^{n+1}$
17:    **if** $dt < dt_{min}$:
18:        Error: algorithm fails to converge

---

5. Numerical validation

We consider three test cases to evaluate the performance of the numerical methods described in the previous sections. The first one, presented in Section 5.1, is a 2D domain with one single fracture. It is divided into three sub-cases in which the fracture orientation and rock properties are modified. The second case, reported in Section 5.2, involves a fracture network composed of 10 fractures with different permeability, some of which intersect. In the last test case, shown in Section 5.3, we study a 3D geometry cut by 8 fractures with multiple intersections.

To keep the presentation simple, we apply the same fluid properties to the two phases for all test cases: the heavy phase, denoted by the subscript 0, has a density $\rho_0 = 1$ and dynamic viscosity $\mu_0 = 1$, the light phase is described by $\rho_1 = 0.5$ and $\mu_1 = 1$.

In all the cases, unless otherwise specified, we use the following convention to define the dimensionless groups E_A as in (4): the reference values are related to the matrix domain where L_{ref} is the vertical length and ρ_{ref} is the difference of the densities of the two phases and Φ_{ref} is the porosity of the matrix domain.

The primary criteria to compare the discussed numerical schemes are the number of Newton iterations done, being a proxy of the associated computational cost, and the accuracy to compute the numerical solution. Other specific results are described case by case.

The iterative method is stopped when the error, *err*, defined as the norm of the normalized ℓ_2-norm of the increment, δx, is smaller than a given tolerance:

$$err = \frac{\|\delta x\|_2}{\sqrt{\dim \delta x}} < tol,$$

where $\dim \delta x$ is the size of the vector δx. Unless differently specified, we set tolerance equal to $tol = 10^{-6}$.

5.1. Case 1. Single fracture

The first test considers a simple 2D unit square domain, Fig. 3, and aims to study the main characteristics of the discretization methods. We investigate three sub-cases by varying the position of the fracture, its permeability, and the grid elements shape (triangles or squares), see Fig. 3. In particular, *Case 1.a* has an horizontal fracture touching both borders, *Case 1.b* has a vertical highly permeable fracture that ends inside the matrix, the last one *Case 1.c* has an oblique fracture.

The dynamic is defined by the unstable initial condition with the heavy phase on the top and the light one on the bottom, separated by a sharp front and forced by the gravity, as depicted, for example, in Fig. 7.

5.1.1. Case 1.a. Horizontal fracture

The parameters and properties used in this case are summarized in Table 1. The flow motion is strongly dependent on the permeability of the fracture that crosses the entire domain, since the two halves of the domain only interact through the mortar fluxes.

The computational grid is made of square elements, as depicted in Fig. 3, with a limited number of elements, whose edge length is 0.05.
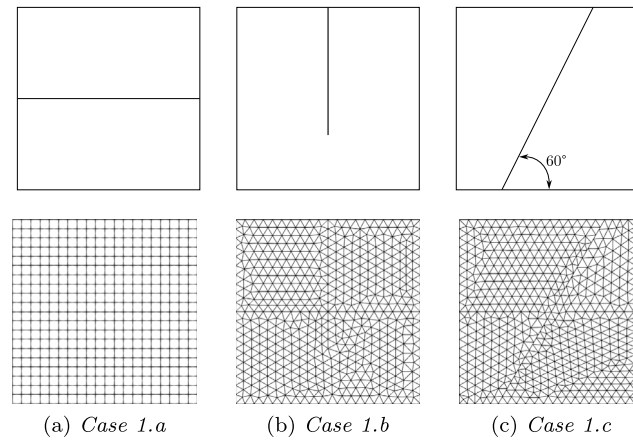
(a) *Case 1.a*   (b) *Case 1.b*   (c) *Case 1.c*

Fig. 3. Case 1. Domains and grids for the example in Section 5.1. The fracture is located in three different positions, (a) horizontally with tips touching the borders, (b) vertically with one tip touching the border and the other immersed in the matrix, (c) with an angle and the tips touching the borders. Different types of grid are used: (a) structured with quadrilateral elements, (b) unstructured with triangular elements, (c) unstructured nonconforming at the fracture interface with triangular elements.

Table 1
Case 1. Horizontal. Parameters used for this problem.

Matrix intrinsic permeability	$K_2 = 1$
Fracture intrinsic permeability	$K_1 = 1$
Fracture normal permeability	$k_{\perp,1} = 0.1$
Fracture codimension extension (aperture)	$\varepsilon_1 = 0.01$
Matrix porosity	$\Phi_2 = 0.25$
Fracture porosity	$\Phi_1 = 0.25$
Total simulation time	$T = 20$
Timestep max	$\Delta t_{max} = 0.4$
E_A	0.0625

The cumulative number of Newton iterations versus the simulation time is shown in the right column of Fig. 4. Due to the simplicity of the test case here a minor advantage is provided by the HU regarding the cumulative number of Newton iterations. Moreover, in the same picture, we show the cumulative number of Newton iterations for a finer grid, whose cell edge length is 0.025. The results remain consistent, in particular, the HU performs better and the gap in the performance increases, suggesting stability in the results as the grid is refined. In the same picture, we can see the time-cumulative number of wasted flips of the upwind direction, summed over all the grid faces of the domain. Unless differently specified, only the 2D domain is shown, since it is the one that affects the Newton iteration the most. In particular, for the PPU the upwind directions are linked to the volumetric fluxes, q_0 and q_1, that are more prone to change during the Newton iterations. For the HU the directions are determined by the total velocity, q_T, and the gravity related function ω_0, that is very stable throughout the simulation. The middle panel of Fig. 4 shows the cumulative number of timestep reductions; see Section 4.5. For this particular case, no cuts are performed.

Note that the two methods behave differently in the presence of a sharp saturation front. In particular, the HU method is more diffusive than the PPU, as shown in Fig. 5(a) that represents the saturation profile along a vertical line during the transient. A sharp increase in saturation is visible at $y = 0.5$ due to the presence of the fracture. The behavior near the fracture is similar for both PPU and HU since the fluxes at the interface boundaries are computed with the same discretization scheme, see Section 4.

5.1.2. Case 1.b. Vertical fracture

The parameters and properties defining this case are summarized in Table 2.

The flow in the high-permeability fracture is faster than that in the surrounding materials, so the fracture drains the heavy fluid from the top and releases it at the bottom. From a numerical standpoint, this implies a significant difference of flows inside and outside the fracture, exploiting the mortar fluxes for the absorption and release of fluid in fracture.

Indeed, observing Fig. 6, which shows the saturation along a vertical line near, but not coincident with, the fracture in the 2D domain, we can see, at time $t = 0.3$, a formation of a local minimum of the saturation located at the top (absorption) and a local maximum at the inner tip of the fracture, at $y = 0.3$ (release).

Results regarding the iterative methods, Fig. 4, are similar to the ones of the previous case.

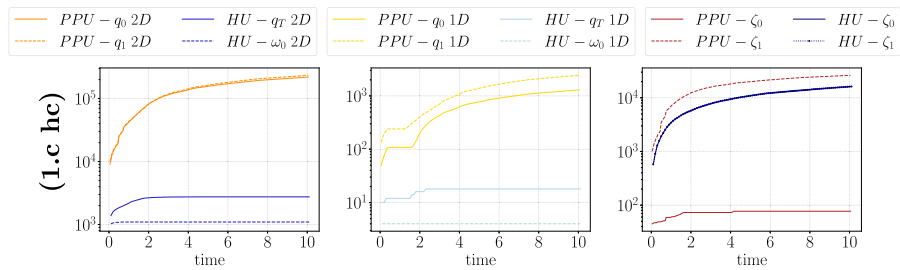### 5.1.3. Case 1.c. Slanted fracture, non-conforming grid

The parameters and properties defining this case are summarized in Table 3.
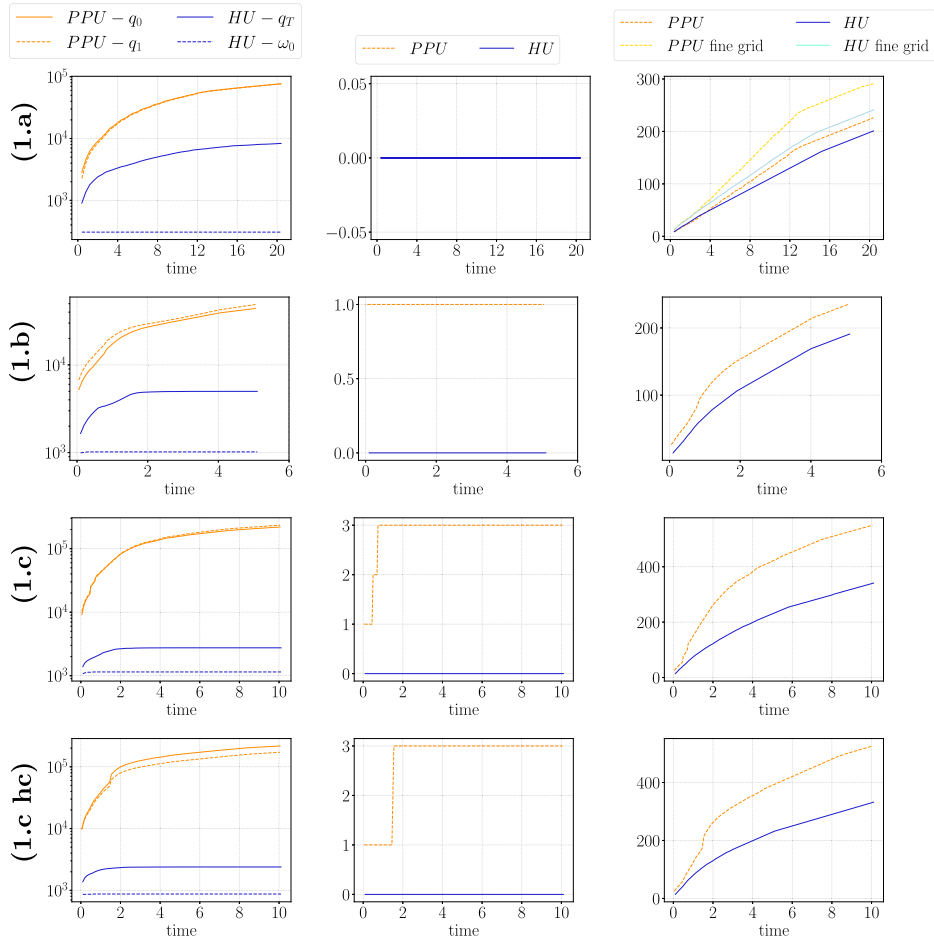
Cumulative number of flips of the upwind directions.

Cumulative number of time cuts.

Cumulative number of Newton iterations.

Cumulative number of flips of the upwind directions for *Case 1.c.* 2D domain on the left panel, 1D domain at the center, mortar on the right.

Fig. 4. Case 1. Characteristics regarding the iterative method.

The normal permeability $k_\perp$ of the fracture is low so it creates an obstacle to the flow through it. Indeed, in Fig. 7 we can see that the phases tend to slide along the fracture before reaching the stationary condition where the two phases have swapped position with respect to the initial condition.

13
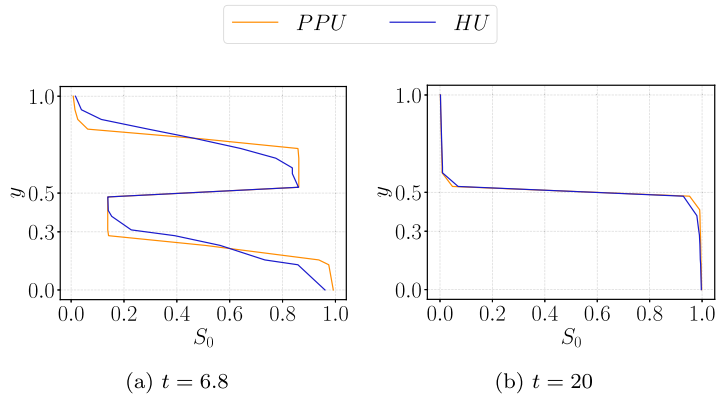
Fig. 5. Case 1. Horizontal. Saturation profile along a vertical line. The left panel illustrates S_0 at time $t = 6.8$, during the countercurrent flow of the two phases. A more diffusive trend is observable for the HU scheme than the PPU. In the right panel, showing the stationary solution at $t = 20$, the lines nearly coincide. No visible differences in the numerical diffusion are appreciable at the discontinuity since the interface fluxes are discretized with the same scheme.

Table 2
Case 1. Vertical. Parameters used for this problem.

Matrix intrinsic permeability	$K_2 = 1$
Fracture intrinsic permeability	$K_1 = 10$
Fracture normal permeability	$k_{\perp,1} = 0.1$
Fracture codimension extension (aperture)	$\varepsilon_1 = 0.01$
Matrix porosity	$\Phi_2 = 0.25$
Fracture porosity	$\Phi_1 = 0.25$
Total simulation time	$T = 5$
Timestep max	$\Delta t_{max} = 0.1$
E_A	0.0625
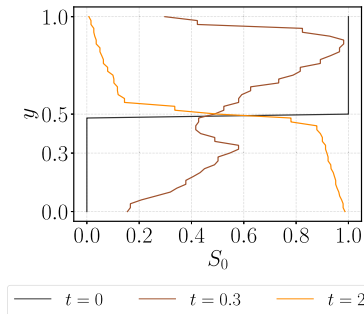
Fig. 6. Case 1. Vertical. Saturation at different timesteps along a vertical line at the center of the 2D domain. At initial time, $t = 0$ a jump along y is prescribed to the saturation, then the fluid is allowed to flow forced by the gravity. At $t = 0.3$ we see the impact of the high permeable fracture, that drains the phase 0 from the top and releases it on the bottom tip around $y = 0.3$. As the stationary condition is approached, $t = 2$, the two phases are separated and they occupy half of the domain each.

We discretized the domain with a simplex non-conforming grid the interface, as visible in Fig. 8. The grid is derived by deforming a conforming grid using a technique that relies on radial basis functions, detailed in [62].

This setup is numerically more challenging than the previous, due to the direction of the fracture, which results in gravity having both an orthogonal and parallel component to the fracture line. Additionally, the non-conforming grid implies a full use of the maps Π and Ξ, that are not identity matrices. Indeed, a greater gap in the performance is visible in Fig. 4.

For this case, we also show the number of wasted flips of the upwind direction for each subdomain and mortar, bottom panel of Fig. 4. The 2D and 1D domains exhibit similar trends, with the HU method showing fewer changes in direction. The behavior of the upwind across domains, which is the same for both PPU and HU, varies according to the upwind discretization method used in the neighboring domains and there is no evident improvement in the HU case. This suggests that a hybrid upwind between domains could lead to advantages. By comparing these graphs with those showing the cumulative number of Newton iterations, we notice that the Newton iterations are predominantly influenced by the flips in the 2D domain.

Furthermore, increasing the permeability contrast in the 1D and 2D domains does not significantly affect the characteristics of the iterative method. The results are shown in Fig. 4 *Case 1.c* and *Case 1.c hc* (high contrast) where the permeabilities of the fracture

Table 3
Case 1. Slanted fracture. Parameters used in this problem.

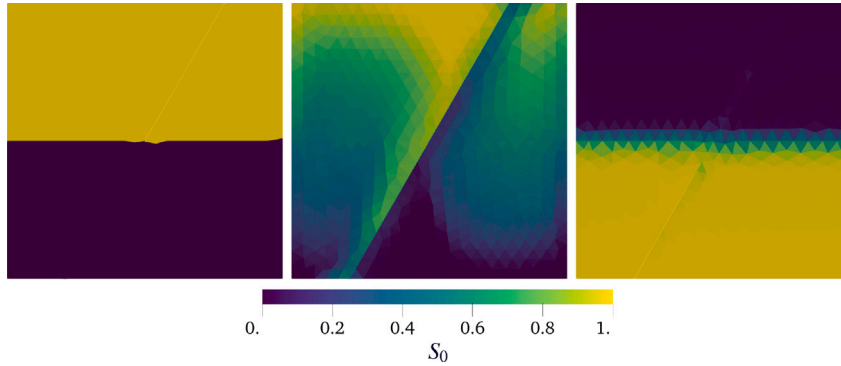| Matrix intrinsic permeability	$K_2 = 1$
Fracture intrinsic permeability	$K_1 = 1$
Fracture normal permeability	$k_{\perp,1} = 0.01$
Fracture codimension extension (aperture)	$\varepsilon_1 = 0.01$
Matrix porosity	$\Phi_2 = 0.25$
Fracture porosity	$\Phi_1 = 0.25$
Total simulation time	$T = 10$
Timestep max	$\Delta t_{max} = 0.1$
E_A	0.0625

Fig. 7. Case 1. Slanted fracture. Three time instances, on the left we have the initial condition in which the heavy phase (denoted by subscript 0) occupies the upper half of the domain and the light phase occupies the lower part. A non perfectly straight interface is due to the irregularity of the mesh. The middle panel shows the saturation distribution at a later time. We can clearly see the effects of the low-permeable fracture that generates a jump in the saturation value. On the right is the stationary condition, where the phases have swapped positions.
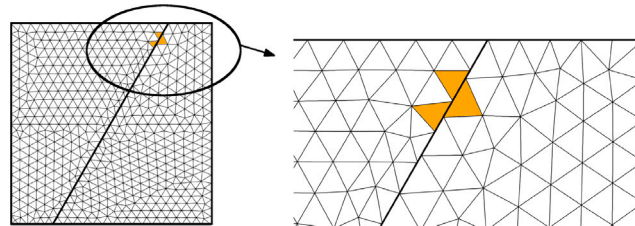

Fig. 8. Case 1. Slanted fracture. Zoom on the simplex grid of the 2D domain. The orange elements highlight the lack of conformity at the fracture interface. (For interpretation of the references to color in this figure legend, the reader is referred to the web version of this article.)

are $k_1 = 10^{-6}$ and $K_\perp = 10^{-8}$. For *Case 1.c*, the bottom panel of Fig. 4 displays the cumulative number of upwind direction flips for both 2D and 1D domains, as well as for the mortar.

We perform a spatial convergence analysis of the HU method, comparing the solution obtained with a reference conforming grid, Fig. 9. The analysis is performed by calculating a single time step from a smooth solution in the primary variables and then calculating the L^2-norm of the spatial error with respect to a reference solution computed with the HU on a very fine grid. For this test case, we observe that the error slopes for both pressure and saturation are proportional to h, while for the mortar the error graphically decreases as $h^{3/2}$. Increasing the value of the normal permeability to $k_{\perp,1} = 10$, thus making the mortar fluxes larger, we observe a convergence rate proportional to h for all the variables, Fig. 9 bottom row.

The nonconforming grid allows to exploit the full capabilities of the dual-mortar formulation, demonstrating that there are no significant differences on the error using a conforming grid, thus with identity maps, Π and Ξ, or a nonconforming grid.

Thanks to the finite volume method, conservative by construction, the mass of the two phases remains perfectly conserved throughout the entire simulation, as illustrated in Fig. 10. Equivalent results are obtained for all the other tests, so they will not be shown.

5.2. Case 2. Complex fracture network

The geometry of this test case is taken from [72]. The presence of many fractures, with intersections of X-type or L-type (fracture 5 and 6) as shown in Fig. 11, and the resulting formation of 0D domains, adds a significant challenge to this test. Fractures number
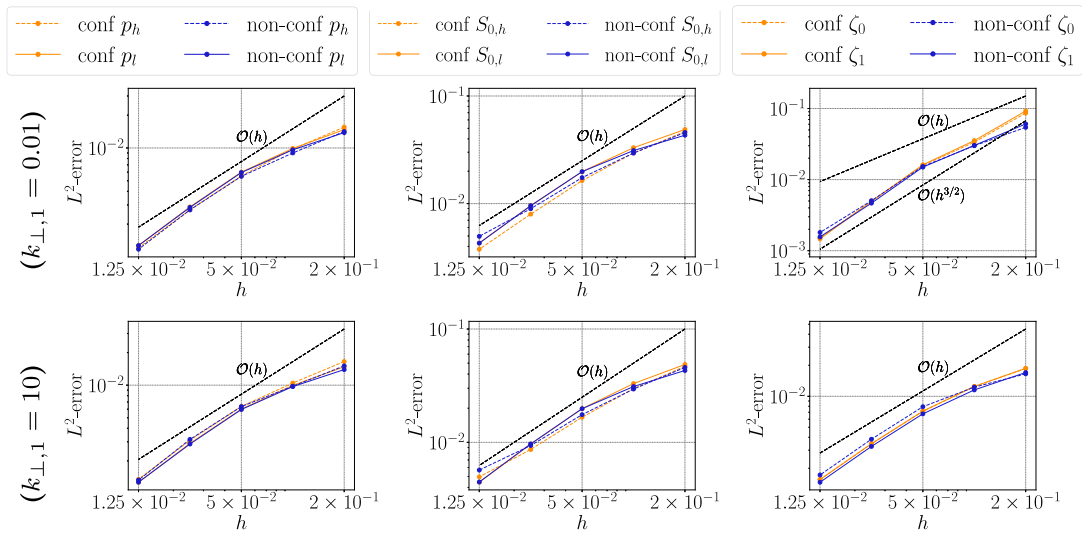
Fig. 9. Case 1. Slanted. Spatial convergence on a conforming grid and non-conforming grid. The first row shows the grid convergence for the default value of the normal permeability, $k_{\perp,1}$. In this case, the mortar fluxes are small due to the low permeability, and the related curve shows alignment to $h^{3/2}$. The second row shows the grid convergence for an increased value of the normal permeability, namely $k_{\perp,1} = 10$. The curve related to the mortar fluxes is aligned to h.
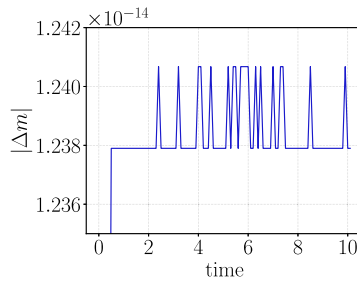

Fig. 10. Case 1. Slanted. Variation of the total mass of phase 0 versus time. The variation is referred to the initial mass, so at initial time the variation is 0 and it does not fit the axis range. The initial mass is 0.127. Thanks to the finite volume method, the mass is conserved at each timestep.

4 and 5 have low permeability, while the other fractures are highly permeable. The permeability of the intersections are set equal to the harmonic average of the intersecting fractures. The parameters and properties defining this case are summarized in Table 4.

The low-permeable fractures in addition to creating a barrier, retain the fluid by allowing a slow displacement inside them, as depicted in Fig. 11. While in the permeable fractures the saturation values is similar to the one of the surrounding matrix, in the impermeable fractures the saturation distribution is similar to the distribution at the initial time.

The cumulative number of flips of the upwind direction, the number of timestep reductions and cumulative Newton iteration, Fig. 12, show the better performance of HU compared to PPU, in particular, the latter requires a number of timesteps cuts up to 4 per time step, causing a large amount of wasted iterations. Indeed, the end of the simulation, the number of iterations required by HU is approximately three times lower. The simulation thus showed that HU significantly outperforms PPU also for more complex geometries.

5.3. Case 3. Network with small features

The geometry and the domain are replicated from [26]. We list in Table 5 the main properties. For this case, we set the Newton tolerance $tol = 2 \times 10^{-5}$. The fracture network is high permeable whereas the surrounding matrix is low permeable. Fig. 13 illustrates the 2D fracture network immersed in a 3D domain. The fracture intersection are of X and Y-type with small angles. This complicated geometry entails the generation of ill-shaped grid elements, a challenge for the discretization methods, Fig. 13.

As in the previous case, we set the heavy phase to lay initially in the top part of the domain and the motion is then forced by the gravity. The permeability contrast produces a fast dynamics in the fracture that lasts till around time 0.1 before a slow motion takes place in the whole domain till the end of the simulation, we can appreciate the different speed of diffusion inside the fracture and in the matrix due to different E_A numbers, 11.25 for the matrix and 875 for the fracture. In Fig. 13 the saturation during the transient is shown. A small diffusion is visible in the 3D domain, while a large displacement of the phases occurred in the fracture

Table 4

Case 2. Parameters used for this problem. The intersection normal permeability is the harmonic average of the intersecting fractures Γ_j and Γ_q.

Matrix intrinsic permeability	$K_{11} = 100$
Fracture $i \neq 4, 5$ intrinsic permeability	$K_i = 100$
Fracture 4 intrinsic permeability	$K_4 = 0.01$
Fracture 5 intrinsic permeability	$K_5 = 0.01$
Fracture $i \neq 4, 5$ normal permeability	$k_{\perp,i} = 100$
Fracture 4 normal permeability	$k_{\perp,4} = 0.01$
Fracture 5 normal permeability	$k_{\perp,5} = 0.01$
Intersection normal permeability	$k_{\perp,i} = \frac{1}{1/k_{\perp,j} + 1/k_{\perp,q}}$
Fracture codimension extension (aperture)	$\varepsilon_i = 0.01$
Intersection codimension extension (area)	$\varepsilon_i^2 = 0.01^2$
Matrix porosity	$\Phi_{11} = 0.25$
Fracture porosity	$\Phi_i = 0.25$
Intersection porosity	$\Phi_i = 0.25$
Total simulation time	$T = 0.05$
Timestep max	$\Delta t_{max} = 2 \times 10^{-3}$
E_A	6.25

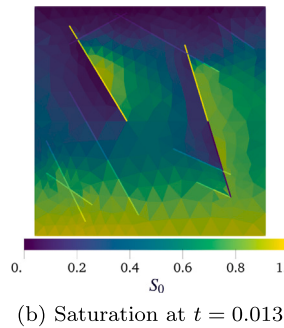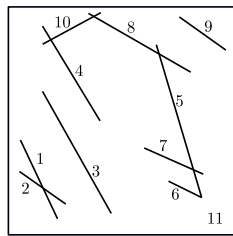(a) Fracture network

(b) Saturation at $t = 0.013$

Fig. 11. Case 2. (a) Domain. The fracture network geometry is taken from [72]. (b) Saturation at time $t = 0.013$. The profiles of the saturation in the high-permeable fractures adjust to the surrounding domain. Instead, the low-permeable fracture permit a small motion of fluid across and along them.
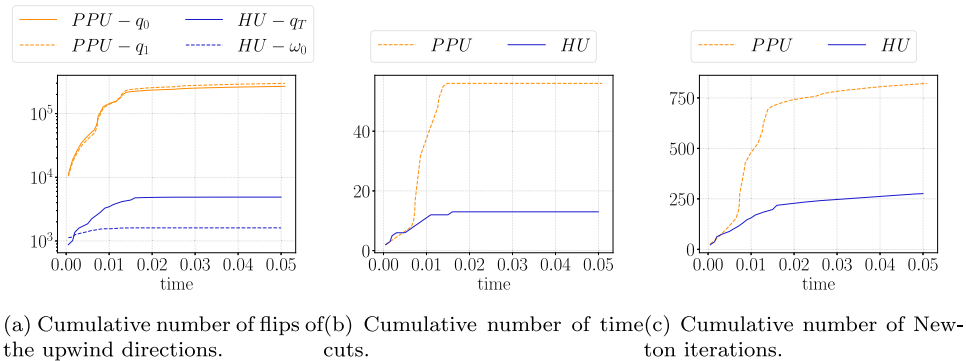

(a) Cumulative number of flips of the upwind directions.

(b) Cumulative number of time cuts.

(c) Cumulative number of Newton iterations.

Fig. 12. Case 2. Characteristics regarding the iterative method.

network. Results in Fig. 14 show that the PPU fails to converge at the beginning of the simulation, during the fast dynamics, while the increased robustness of HU enabled this challenging simulation to be completed with a limited number of time step cuts.

6. Conclusion

We address the physical problem of two-phase flow in the subsurface with a fractured matrix rock. We model fractures, and possibly intersections, through a dimensionally reduced object obtaining a mixed-dimensional domain. The fluid motion is governed by partial derivative equations defined in each subdomain, while the interaction between the subdomains is described by Lagrange multipliers that are represented by fluid fluxes. The fluid flow is dictated by possible sources/wells, boundary conditions and, most

Table 5
Case 3. Parameters defining the test case.

Matrix intrinsic permeability	$K_3 = 100$
Fracture i intrinsic permeability	$K_i = 10^4$
Intersection i intrinsic permeability	$K_i = 10^4$
Fracture i normal permeability	$k_{\perp,i} = 10^4$
Intersection i normal permeability	$k_{\perp,i} = 10^4$
Fracture codimension extension (aperture)	$\varepsilon_i = 0.01$
Intersection codimension extension (area)	$\varepsilon_i^2 = 0.01^2$
Matrix porosity	$\Phi_3 = 0.2$
Fracture porosity	$\Phi_i = 0.2$
Intersection porosity	$\Phi_i = 0.2$
Total simulation time	$T = 0.01$
Timestep max	$\Delta t_{max} = 10^{-5}$
Newton tolerance	$tol = 2 \times 10^{-5}$
E_A	11.25

(a) Fracture network   (b) Ill-shaped cells   (c) $t = 1.3 \times 10^{-3}$ (d) $t = 2.86 \times 10^{-3}$
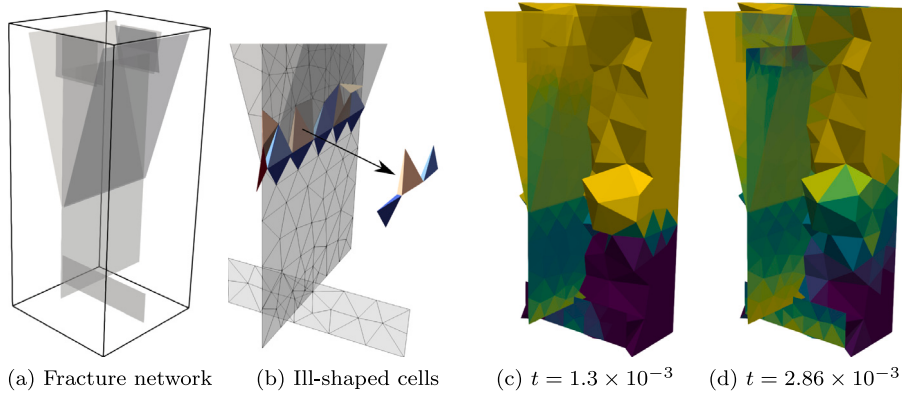
Fig. 13. Case 3. (a) Domain and fracture network. (b) The fracture configuration with narrow angles leads to ill-shaped grid elements. The highlighted elements have a ratio of the circumscribed and inscribed sphere radius between 3.5 and 4.1. (c) and (d) Saturation at time $t = 1.3 \times 10^{-4}$ and $t = 2.86 \times 10^{-3}$, respectively. We can appreciate different time scales due to different E_A numbers, specifically 11.25 in the matrix and 875 in the fracture, the fast one inside the fractures and the slow one in the 3D domain. Some fractures are made partially transparent for graphical reason.
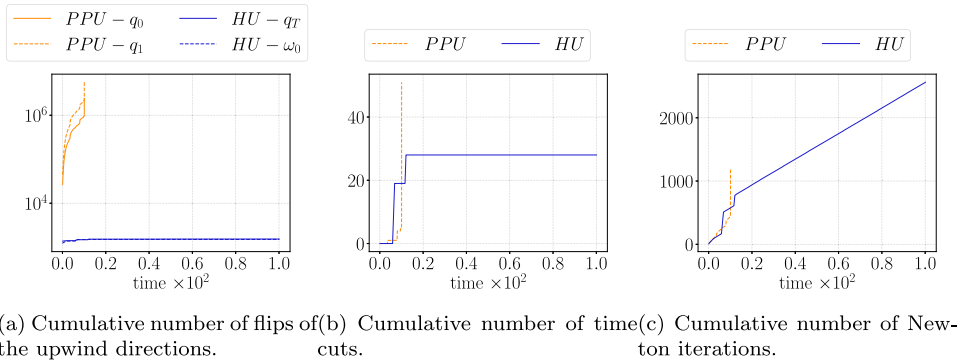

(a) Cumulative number of flips of the upwind directions.   (b) Cumulative number of time cuts.   (c) Cumulative number of Newton iterations.

Fig. 14. Case 3. Characteristics regarding the iterative method. The PPU method fails to converge up to a reasonable timestep size while the HU proves to be more robust.

importantly, gravity. This configuration is known to generate countercurrent flows, a condition that spoils the performance of the nonlinear solver (Newton).

We tackle the convergence problem by working on the discretization of the fluxes. We then extended the work done in [44] on a hybrid upwind strategy to the case of a mixed-dimensional framework. We implement the method in PorePy, a simulation tool for fractured and deformable porous media suitable for the mixed-dimensional problem [71].

We test the discretization method on three different geometries, both 2D and 3D, with intersecting fracture network, discretized with simplex and hexahedral meshes, and we test the method on different flow regimes, imposed by different rock properties. We show numerically the convergence of the method, even with non-conforming grids at subdomain interfaces. In each test case, the

proposed method reduces the number of Newton iterations. In particular, in the third case (Section 5.3), the standard discretization method fails to converge, making it impossible to complete the time-dependent simulation. On the other hand, an increase in numerical diffusion is observed.

Given the promising results obtained, further developments will be undertaken, such as, from the physical point of view, extension to n-phases, high compressible fluids, inclusion of capillary effects and chemical reactions. From the numerical point of view, a hybrid upwind strategy should also be adopted at the interfaces to further improve performance, in addition to a study aimed at decreasing the numerical diffusion added by the discretization method. Moreover, despite an increment in the computational cost for solving the linear system, we expect an improvement in the accuracy by using of MPFA and gravity consistent transmissibilities in (20) instead of TPFA.

The numerical scheme has been shown to be robust and effective in reducing the number of Newton iterations, resulting in benefits in the computational cost of the simulation.

CRediT authorship contribution statement

Enrico Ballini: Writing – review & editing, Writing – original draft, Validation, Software, Methodology, Formal analysis, Conceptualization. **Luca Formaggia:** Writing – review & editing, Supervision. **Alessio Fumagalli:** Writing – review & editing, Writing – original draft, Validation, Supervision. **Eirik Keilegavlen:** Writing – review & editing, Writing – original draft, Validation, Supervision, Conceptualization. **Anna Scotti:** Writing – review & editing, Validation, Supervision.

Declaration of competing interest

The authors declare that they have no known competing financial interests or personal relationships that could have appeared to influence the work reported in this paper.

Data availability

Data will be made available on request.

Acknowledgments

References

[1] M. Iding, P. Ringrose, Evaluating the impact of fractures on the performance of the in salah CO2 storage site, Int. J. Greenh. Gas Control 4 (2) (2010) 242–248.
[2] C.-F. Tsang, I. Neretnieks, Y. Tsang, Hydrologic issues associated with nuclear waste repositories, Water Resour. Res. 51 (9) (2015) 6923–6972.
[3] C. Lister, On the penetration of water into hot rock, Geophys. J. Int. 39 (3) (1974) 465–509.
[4] T. Fujiwara, J. Lin, T. Matsumoto, P.B. Kelemen, B.E. Tucholke, J.F. Casey, Crustal evolution of the Mid-Atlantic Ridge near the Fifteen-Twenty fracture zone in the last 5 Ma, Geochem. Geophys. Geosyst. 4 (3) (2003).
[5] E. Bonnet, O. Bour, N.E. Odling, P. Davy, I. Main, P. Cowie, B. Berkowitz, Scaling of fracture systems in geological media, Rev. Geophys. 39 (3) (2001) 347–383.
[6] I. Berre, F. Doster, E. Keilegavlen, Flow in fractured porous media: A review of conceptual models and discretization approaches, Transp. Porous Media 130 (1) (2019) 215–236.
[7] M. Karimi-Fard, B. Gong, L.J. Durlofsky, Generation of coarse-scale continuum flow models from detailed fracture characterizations, Water Resour. Res. 42 (10) (2006).
[8] B. Gong, M. Karimi-Fard, L.J. Durlofsky, Upscaling discrete fracture characterizations to dual-porosity, dual-permeability models for efficient simulation of flow with strong gravitational effects, Spe J. 13 (01) (2008) 58–67.
[9] S. Geiger, M. Dentz, I. Neuweiler, A novel multirate dual-porosity model for improved simulation of fractured and multiporosity reservoirs, SPE J. 18 (04) (2013) 670–684.
[10] S.H. Lee, M. Lough, C. Jensen, Hierarchical modeling of flow in naturally fractured formations with multiple length scales, Water Resour. Res. 37 (3) (2001) 443–455.
[11] A. Fumagalli, L. Pasquale, S. Zonca, S. Micheletti, An upscaling procedure for fractured reservoirs with embedded grids, Water Resour. Res. 52 (8) (2016) 6506–6525.
[12] M. Ţene, S.B. Bosma, M.S. Al Kobaisi, H. Hajibeygi, Projection-based embedded discrete fracture model (pEDFM), Adv. Water Resour. 105 (2017) 205–216.
[13] L. Li, S.H. Lee, Efficient field-scale simulation of black oil in a naturally fractured reservoir through discrete fracture networks and homogenized media, SPE Reserv. Eval. Eng. 11 (04) (2008) 750–758.
[14] V. Martin, J. Jaffré, J.E. Roberts, Modeling fractures and barriers as interfaces for flow in porous media, SIAM J. Scient. Comput. 26 (5) (2005) 1667–1691.
[15] S. Mishra, J. Jaffré, On the upstream mobility scheme for two-phase flow in porous media, Comput. Geosci. 14 (1) (2010) 105–124.
[16] J. Jaffré, M. Mnejja, J.E. Roberts, A discrete fracture model for two-phase flow with matrix-fracture interaction, in: Proceedings of the International Conference on Computational Science, ICCS 2011, Procedia Comput. Sci. 4 (2011) 967–973.
[17] A. Fumagalli, A. Scotti, A numerical method for two-phase flow in fractured porous media with non-matching grids, Adv. Water Resour. 62, Part C (2013) 454–464, Computational Methods in Geologic CO2 Sequestration.

[18] R. Ahmed, M.G. Edwards, S. Lamine, B.A.H. Huisman, M. Pal, Control-volume distributed multi-point flux approximation coupled with a lower-dimensional fracture model, J. Comput. Phys. 284 (2015) 462–489.

[19] K. Brenner, M. Groza, C. Guichard, R. Masson, Vertex approximate gradient scheme for hybrid dimensional two-phase Darcy flows in fractured porous media, ESAIM Math. Model. Numer. Anal. 49 (2) (2015) 303–330.

[20] K. Brenner, J. Hennicker, R. Masson, P. Samier, Gradient discretization of hybrid-dimensional Darcy flow in fractured porous media with discontinuous pressures at matrix-fracture interfaces, IMA J. Numer. Anal. (2016).

[21] E. Ahmed, J. Jaffré, J.E. Roberts, A reduced fracture model for two-phase flow with different rock types, Math. Comput. Simulation 137 (2017) 49–70, MAMERN VI-2015: 6th International Conference on Approximation Methods and Numerical Modeling in Environment and Natural Resources.

[22] K. Brenner, J. Hennicker, R. Masson, P. Samier, Hybrid-dimensional modelling of two-phase flow through fractured porous media with enhanced matrix fracture transmission conditions, J. Comput. Phys. 357 (2018) 100–124.

[23] W.M. Boon, J.M. Nordbotten, I. Yotov, Robust discretization of flow in fractured porous media, SIAM J. Numer. Anal. 56 (4) (2018) 2203–2233.

[24] A. Fumagalli, A. Scotti, A reduced model for flow and transport in fractured porous media with non-matching grids, in: A. Cangiani, R.L. Davidchack, E. Georgoulis, A.N. Gorban, J. Levesley, M.V. Tretyakov (Eds.), Numerical Mathematics and Advanced Applications 2011, Springer Berlin Heidelberg, 2013, pp. 499–507.

[25] A. Fumagalli, A. Scotti, A mathematical model for thermal single-phase flow and reactive transport in fractured porous media, J. Comput. Phys. 434 (2021).

[26] I. Berre, W.M. Boon, B. Flemisch, A. Fumagalli, D. Gläser, E. Keilegavlen, A. Scotti, I. Stefansson, A. Tatomir, K. Brenner, S. Burbulla, P. Devloo, O. Duran, M. Favino, J. Hennicker, I.-H. Lee, K. Lipnikov, R. Masson, K. Mosthaf, M.G.C. Nestola, C.-F. Ni, K. Nikitin, P. Schädle, D. Svyatskiy, R. Yanbarisov, P. Zulian, Verification benchmarks for single-phase flow in three-dimensional fractured porous media, Adv. Water Resour. 147 (2021) 103759.

[27] R.L. Berge, I. Berre, E. Keilegavlen, J.M. Nordbotten, Numerical simulations of viscous fingering in fractured porous media, Transp. Porous Media 151 (7) (2024) 1511–1538.

[28] T. Garipov, M. Karimi-Fard, H. Tchelepi, Discrete fracture model for coupled flow and geomechanics, Comput. Geosci. 20 (2016) 149–160.

[29] I. Stefansson, I. Berre, E. Keilegavlen, A fully coupled numerical model of thermo-hydro-mechanical processes and fracture contact mechanics in porous media, Comput. Methods Appl. Mech. Engrg. 386 (2021) 114122.

[30] A. Novikov, D. Voskov, M. Khait, H. Hajibeygi, J.D. Jansen, A scalable collocated finite volume scheme for simulation of induced fault slip, J. Comput. Phys. 469 (2022) 111598.

[31] D. Gläser, R. Helmig, B. Flemisch, H. Class, A discrete fracture model for two-phase flow in fractured porous media, Adv. Water Resour. 110 (2017) 335–348.

[32] J.A. Trangenstein, J.B. Bell, Mathematical structure of compositional reservoir simulation, SIAM J. Sci. Stat. Comput. 10 (5) (1989) 817–845.

[33] A.F. Rasmussen, T.H. Sandve, K. Bao, A. Lauser, J. Hove, B. Skaflestad, R. Klöfkorn, M. Blatt, A.B. Rustad, O. Sævareid, et al., The open porous media flow reservoir simulator, Comput. Math. Appl. 81 (2021) 159–185.

[34] Y. Brenier, J. Jaffré, Upstream differencing for multiphase flow in reservoir simulation, SIAM J. Numer. Anal. 28 (3) (1991) 685–696.

[35] B. Li, H.A. Tchelepi, Nonlinear analysis of multiphase transport in porous media in the presence of viscous, buoyancy, and capillary forces, J. Comput. Phys. 297 (2015) 104–131.

[36] X. Wang, H.A. Tchelepi, Trust-region based solver for nonlinear transport in heterogeneous porous media, J. Comput. Phys. 253 (2013) 114–137.

[37] O. Møyner, Nonlinear solver for three-phase transport problems based on approximate trust regions, Comput. Geosci. 21 (5) (2017) 999–1021.

[38] F. Kwok, H. Tchelepi, Potential-based reduced Newton algorithm for nonlinear multiphase flow in porous media, J. Comput. Phys. 227 (1) (2007) 706–727.

[39] J.R. Natvig, K.-A. Lie, Fast computation of multiphase flow in porous media by implicit discontinuous Galerkin schemes with optimal ordering of elements, J. Comput. Phys. 227 (24) (2008) 10108–10124.

[40] S. Lee, Y. Efendiev, H. Tchelepi, Hybrid upwind discretization of nonlinear two-phase flow with gravity, Adv. Water Resour. 82 (2015) 27–38.

[41] F.P. Hamon, H.A. Tchelepi, Analysis of hybrid upwinding for fully-implicit simulation of three-phase flow with gravity, SIAM J. Numer. Anal. 54 (3) (2016) 1682–1712.

[42] F.P. Hamon, B.T. Mallison, H.A. Tchelepi, Implicit Hybrid Upwind scheme for coupled multiphase flow and transport with buoyancy, Comput. Methods Appl. Mech. Engrg. 311 (2016) 599–624.

[43] A.H. Alali, F.P. Hamon, B.T. Mallison, H.A. Tchelepi, Finite-volume simulation of capillary-dominated flow in matrix-fracture systems using interface conditions, Comput. Geosci. 25 (2021) 17–33.

[44] S.B. Bosma, F.P. Hamon, B.T. Mallison, H.A. Tchelepi, Smooth implicit hybrid upwinding for compositional multiphase flow in porous media, Comput. Methods Appl. Mech. Engrg. 388 (2022) 114288.

[45] J.M. Nordbotten, W.M. Boon, A. Fumagalli, E. Keilegavlen, Unified approach to discretization of flow in fractured porous media, Comput. Geosci. 23 (2) (2018) 225–237.

[46] J. Bear, Dynamics of fluids in porous media, American Elsevier Pub. Co., 1972, p. 764.

[47] G. Chavent, J. Jaffré, Mathematical Models and Finite Elements for Reservoir Simulation Single Phase, Multiphase and Multicomponent Flows Through Porous Media, Elsevier Science & Technology Books, 1986.

[48] R. Helmig, Multiphase Flow and Transport Processes in the Subsurface: A Contribution to the Modeling of Hydrosystems, Springer-Verlag, Berlin, Germany, 1997.

[49] J.M. Nordbotten, M.A. Celia, Geological Storage of CO2: Modeling Approaches for Large-Scale Simulation, Wiley, 2011.

[50] R. Brooks, A. Corey, Hydraulic properties of porous media, Hydro Paper 5, Colorado State University, 1964.

[51] J.A. Trangenstein, J.B. Bell, Mathematical structure of the black-oil model for petroleum reservoir simulation, SIAM J. Appl. Math. 49 (3) (1989) 749–783.

[52] E. Buckingham, On physically similar systems; illustrations of the use of dimensional equations, Phys. Rev. 4 (1914) 345–376.

[53] A. Riaz, H. Tchelepi, Stability of two-phase vertical flow in homogeneous porous media, Phys. Fluids 19 (7) (2007).

[54] A. Fumagalli, Numerical Modelling of Flows in Fractured Porous Media by the XFEM Method (Ph.D. thesis), Politecnico di Milano, 2012.

[55] P. Angot, F. Boyer, F. Hubert, Asymptotic and numerical modelling of flows in fractured porous media, ESAIM Math. Model. Numer. Anal. 43 (2) (2009) 239–275.

[56] L. Formaggia, A. Fumagalli, A. Scotti, P. Ruffo, A reduced model for Darcy's problem in networks of fractures, ESAIM Math. Model. Numer. Anal. 48 (4) (2014) 1089–1116.

[57] F.P. Hamon, Implicit Hybrid Upwinding and Advanced Nonlinear Solver for Multiphase Flow and Transport in Porous Media (Ph.D. thesis), Stanford University, 2017.

[58] F.P. Hamon, B.T. Mallison, H.A. Tchelepi, Implicit Hybrid Upwinding for two-phase flow in heterogeneous porous media with buoyancy and capillarity, Comput. Methods Appl. Mech. Engrg. 331 (2018) 701–727.

[59] F.P. Hamon, B.T. Mallison, Fully Implicit multidimensional Hybrid Upwind scheme for coupled flow and transport, Comput. Methods Appl. Mech. Engrg. 358 (2020) 112606.

[60] J. Blazek, in: J. Blazek (Ed.), Computational Fluid Dynamics: Principles and Applications, third ed., Butterworth-Heinemann, Oxford, 2015.

[61] T. Barth, R. Herbin, M. Ohlberger, Finite volume methods: Foundation and analysis, in: Encyclopedia of Computational Mechanics, second Edition, Wiley, 2017, pp. 1–60,

[62] E. Ballini, L. Formaggia, A. Fumagalli, A. Scotti, P. Zunino, Application of deep learning reduced-order modeling for single-phase flow in faulted porous media, Comput. Geosci. (2024).

[63] I. Aavatsmark, An introduction to multipoint flux approximations for quadrilateral grids, Comput. Geosci. 6 (3) (2002) 405–432.

[64] L. Agelas, R. Masson, Convergence of the finite volume MPFA O scheme for heterogeneous anisotropic diffusion problems on general meshes, C.R. Math. 346 (17–18) (2008) 1007–1012.

[65] R.A. Klausen, R. Winther, Convergence of multipoint flux approximations on quadrilateral grids, Numer. Methods Partial Differential Equations 22 (6) (2006) 1438–1454.

[66] I. Aavatsmark, Interpretation of a two-point flux stencil for skew parallelogram grids, Comput. Geosci. 11 (3) (2007) 199–206.

[67] M. Starnoni, I. Berre, E. Keilegavlen, J.M. Nordbotten, Consistent MPFA discretization for flow in the presence of gravity, Water Resour. Res. 55 (12) (2019) 10105–10118.

[68] W. Squire, G. Trapp, Using complex variables to estimate derivatives of real functions, SIAM Rev. 40 (1) (1998) 110–112.

[69] G. Lantoine, R.P. Russell, T. Dargent, Using multicomplex variables for automatic computation of high-order derivatives, ACM Trans. Math. Software 38 (3) (2012) 1–21.

[70] C.H. Bischof, P.D. Hovland, B. Norris, On the implementation of automatic differentiation tools, Higher-Order Symbol. Comput. 21 (3) (2008) 311–331.

[71] E. Keilegavlen, R. Berge, A. Fumagalli, M. Starnoni, I. Stefansson, J. Varela, I. Berre, Porepy: an open-source software for simulation of multiphysics processes in fractured porous media, Comput. Geosci. 25 (1) (2020) 243–265.

[72] B. Flemisch, I. Berre, W. Boon, A. Fumagalli, N. Schwenck, A. Scotti, I. Stefansson, A. Tatomir, Benchmarks for single-phase flow in fractured porous media, Adv. Water Resour. 111 (2018) 239–258.